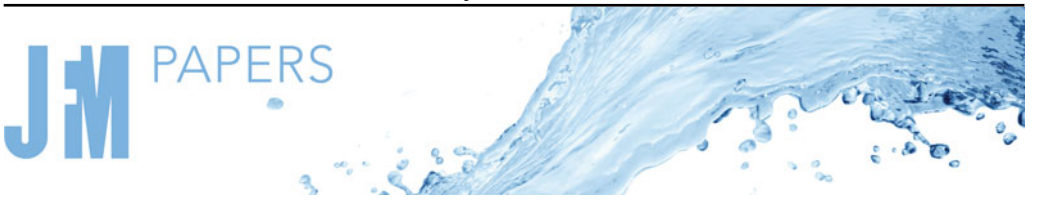
J. Fluid Mech. (2026), *vol.* 1032, A17, doi:10.1017/jfm.2026.11369



Axisymmetric landslides on small planetary bodies

Kumar Gaurav[1] **and Ishan Sharma**[1,2]

[1]Department of Mechanical Engineering, Indian Institute of Technology Kanpur, India

[2]Space Planetary & Astronomical Sciences and Engineering, Indian Institute of Technology Kanpur, India

Corresponding author: Kumar Gaurav, kumgaurav5620@gmail.com

(Received 27 July 2025; revised 24 December 2025; accepted 17 February 2026)

We aim to understand how landslides affect the shape and rotational motion of small rubble planetary bodies. We limit ourselves to axisymmetric global landslides and take the primordial shape of the body to be axisymmetric as well. The landslides are modelled as shallow granular surface flows using depth averaging, while incorporating the effects of the body's rotation, topographical changes from previous landslides, its non-uniform gravity field and possible surface mass shedding. The body's rotational dynamics is coupled to its shape change due to the transport of regolith – surface grains – and also accounts for the influence of radiation torque. We utilise our framework to investigate regolith motion on idealised rubble bodies and actual asteroids. We then study the evolution of the shape and spin state of an initially spherical rubble asteroid undergoing multiple global landsliding events over millions of years – a time scale comparable to typical asteroidal lifetimes. We find that shape changes due to landsliding resist spin-up due to radiation torque and, in some instances, may even cause the body to spin down. Furthermore, rotational fission is delayed, and may even be suppressed, by regolith redistribution toward the body's equator. Finally, top-shaped configurations may emerge rapidly, which may explain the prevalence of top-shaped asteroids in near-Earth orbits.

Key words: avalanches, dry granular material, rotating flows

1. Introduction

Small Solar System bodies, such as sub-kilometre sized near-Earth asteroids (NEAs), are observed to have grain rich – 'sandy' – surfaces, populated mostly by very small grains (fines) and rock, along with several large boulders; see, e.g. the surface of asteroids Bennu and Ryugu in figure 1. This observation may be related to the fact that many of these objects are believed to be 'rubble piles', i.e. they are granular aggregates that are held together primarily by self-gravity (Walsh 2018). Such bodies are generally found to be in

© The Author(s), 2026. Published by Cambridge University Press.

https://doi.org/10.1017/jfm.2026.11369 Published online by Cambridge University Press

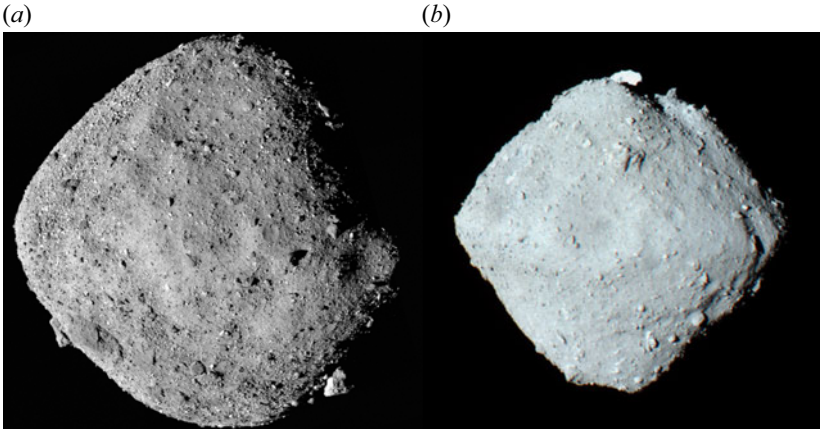


Figure 1. Top-shaped NEAs (*a*) 101955 Bennu and (*b*) 162173 Ryugu. The granular surface is striking with visible rocks and large boulders. Source: NASA and JAXA.

a state of pure rotation about their axis of maximum moment of inertia, because tumbling motion is damped out by internal dissipation (Burns, Safronov & Gold 1973; Sharma, Burns & Hui 2005; Breiter, Rożek & Vokrouhlickỳ 2012). Furthermore, several of them, such as asteroids Bennu and Ryugu in figure 1, have approximately axisymmetric shapes (Barnouin *et al.* 2019; Watanabe *et al.* 2019).

Because such small bodies lack an atmosphere, all impactors, irrespective of their size, are able to reach their surface. Consequently, these bodies experience a large number of impacts during their lifetime and, given their small size, even modest impacts may initiate seismic events that are large enough to cause global landslides (Richardson *et al.* 2005; Quillen *et al.* 2019). At the same time, fast rotation rates, when present, increases the chance of a landsliding event, because centrifugal forces reduce the effective basal pressure. Indeed, morphologies of mass movement on small asteroids have been observed by various missions (Miyamoto *et al.* 2007; Sugita *et al.* 2019; Jawin *et al.* 2020). These mass movements redistribute regolith – surface grains – thereby reshaping and texturing these bodies. This may include erosion of small craters, grain sorting and formation of ridges and terraces. Crucially, shape changes modify the body's mass moment of inertia and also its rotation state in order to conserve the system's angular momentum. Thus, landsliding events over the lifetime of a small Solar System body contribute greatly to changing its shape and rotation state.

The evolution of rubble piles in space has been investigated extensively, employing mainly numerical and experimental techniques. These are surveyed in detail by recent reviews by Walsh (2018) and Hestroffer *et al.* (2019). However, most of these works address the bulk deformation of these object. For example, Walsh, Richardson & Michel (2008) and Sánchez & Scheeres (2012) performed discrete element (DE) simulations to study deformation, disruption and re-accumulation of granular aggregates in space. The finite element method was utilised by Hirabayashi (2015) and Hirabayashi & Scheeres (2019) to probe the structural failure of rubble asteroids, while Sugiura *et al.* (2021) used smooth particle hydrodynamics to follow the deformation of an initially spherical asteroid. More information is available in the reviews cited above. Analytical efforts have been generally limited to estimating incipient failure or finding equilibrium configurations and testing their stability; see, e.g. Sharma (2017).

There is relatively less effort to model regolith motion on the surface of asteroids, which is our focus here. Analytical approaches generally assume idealised shapes. These include

https://doi.org/10.1017/jfm.2026.11369 Published online by Cambridge University Press

the works of Harris, Fahnestock & Pravec (2009) and Scheeres (2015), both of which were fundamentally predicated on the motion of a single particle in the effective geopotential of a spinning body, once a local slope-stability criterion is violated. Similar techniques were utilised to investigate the motion of a single particle or boulder on the surface of an asteroid (Jiang, Zhang & Baoyin 2016; Zhang *et al.* 2019; Brack & McMahon 2019; Huang *et al.* 2022).

Regolith motion on the actual shape of the asteroid has not been studied extensively. Most studies employ DE simulations of granular flow on a spherical rigid core (Hirabayashi, Sánchez & Scheeres 2015; Tardivel, Sánchez & Scheeres 2018; Sánchez & Scheeres 2020; Cheng *et al.* 2021) or on a patch of a rubble asteroid (Tang *et al.* 2023; Ghosh, Sharma & Dhingra 2024). Hirabayashi & Scheeres (2019) utilised finite element (FE) computations to predict the regions of rotational failure on arbitrarily shaped asteroids. Recently, Song *et al.* (2024) integrated their DE code with the shape model of Bennu, incorporating its self-gravity, to simulate regolith flow.

Such simulation efforts are computationally expensive and so are not best suited to study the shape and spin evolution of rubble piles over their lifetime. The primary reason is that events, such as impact-driven landslides, will occur many times over this time period, each one of which will need to be resolved, which takes significant computing time. This motivates the present work, where we model landslides on small planetary bodies by suitably extending continuum models for shallow terrestrial landslides on an arbitrary topography (Savage & Hutter 1989; Gray, Wieland & Hutter 1999; Bouchut & Westdickenberg 2004; Pudasaini & Hutter 2007; Luca, Tai & Kuo 2016). We develop the governing framework in a fairly general setting. Subsequently, we limit ourselves to global axisymmetric landslides on an initially axisymmetric shape, but allow the topography to vary across latitudes. We incorporate the effects of the body's rotation and non-central gravitational field, as well as couple the shape changes and consequent mass redistribution to the body's rotational dynamics.

Previous efforts in this general direction include the work of Richardson *et al.* (2005), who modelled the downslope motion due to seismic shaking, the study of two-dimensional landslides on a rotating ellipse by Gaurav *et al.* (2021) and axisymmetric landslides on a top-shaped rotating body by Banik, Gaurav & Sharma (2022). Here, we extend the latter modelling effort significantly in the following ways: (i) we allow global axisymmetric landsliding on a body whose initial shape is any surface of revolution, (ii) we also update the body's topography after every landslide and (iii) we include the effects of radiation torques on the body's rotational dynamics. This greatly expands the applicability to realistic bodies, as well as paves the way for the fully general case of local landslides on an arbitrarily shaped body. We then apply our model to axisymmetric shapes derived from available shape models of several asteroids to study the motion and final deposition of an initially uniformly distributed layer of regolith. We will also consider the change in shape and spin of an initially spherical asteroid due to multiple landsliding events over the course of its lifetime. Our observations prompt three important hypotheses, *viz.* (*a*) shape changes introduced by regolith flow resist spin up due to radiation torque and may even cause the body to spin down, (*b*) rotational fission – loss of material due to centrifugal effects at high rotation rates – is delayed, and may even be suppressed, by regolith redistribution to the body's equator by landsliding and (*c*) top shapes are rapidly formed and this may explain the prevalence of top-shaped asteroids in near-Earth orbits.

The paper is organised as follows. In § 2, we provide general set of equations that solve for the regolith flow during a landslide and also couple it to the body's rotational dynamics. These are simplified for an axisymmetric system in § 3. We provide illustrative results and applications to real asteroids in § 4, before concluding.

https://doi.org/10.1017/jfm.2026.11369 Published online by Cambridge University Press

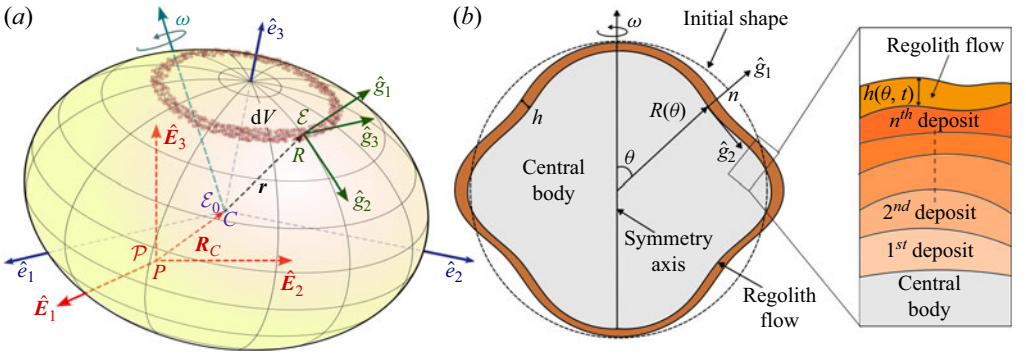


Figure 2. Schematic of a rotating planetary body with angular velocity $\boldsymbol{\omega}$. Three different coordinate systems are indicated and these are discussed in the main text. The differential volume element $\mathrm{d}V$ of an axisymmetric regolith layer is shown. (*b*) The shape of an initially spherical body after multiple global axisymmetric landsliding events. The brown layer depicts an ongoing landslide (regolith flow). The inset shows how landslides are deposited over time over the central body.

2. General governing equations

Figure 2 represents the setting in the context of an initially axisymmetric body in figure 2(*a*) that is rotating at the angular velocity $\boldsymbol{\omega}$. The body is taken to comprise grains that, at any given time, may be broadly distinguished into two regions: a solid central body where grains are consolidated and/or compacted and/or sintered, and a mobile layer of regolith that arises when landslides occur, as shown in figure 2(*b*). On the other hand, in between two landsliding events the entire body will be the central body. The shape and size of the central body is thus modified when regolith is mobilised, flows and stops. We incorporate the possibility of multiple landslides initiated, say, by impact events over the course of the body's lifetime, and the inset in figure 2 shows how these landslides deposit over each other.

We now proceed as follows. We will first gather equations that govern regolith flow on a body and couple it to the body's rotational dynamics in a fairly general setting. The flow will be taken to be three-dimensional. We will allow the body's angular velocity to be arbitrarily located, and not necessarily aligned with the body's principal axes of inertia; thus the body may tumble in space. Furthermore, the landslides need not be axisymmetric and thus cause the centre of mass of the body to shift. The rotational dynamics of the system will incorporate effects of the system's changing mass moment of inertia. No specific assumptions will be made on forces and torques acting on the system. We will subsequently introduce assumptions that will simplify the presentation, but will still be useful for realistic applications.

We will employ three coordinate systems shown in figure 2(*a*), *viz.* the inertial coordinate system $\{\mathcal{P}, P, \hat{\boldsymbol{E}}_i\}$ with origin at some space-fixed point P and unit vectors $\hat{\boldsymbol{E}}_i$; the body-fixed coordinate system $\{\mathcal{E}_0, C, \hat{\boldsymbol{e}}_i\}$, which is attached to the central body and is defined by its principal axes $\hat{\boldsymbol{e}}_i$ and C lies at the central body's centre of mass; and $\{\mathcal{E}, R, \hat{\boldsymbol{g}}_i\}$ is a curvilinear coordinate system defined by the natural unit basis $\hat{\boldsymbol{g}}_i$ associated with the body's surface. Henceforth, we represent all vector quantities measured in the inertial frame $\mathcal{P}$ and the body-fixed coordinate system by, respectively, bold upper and lower case letters.

A common simplification in the analysis of landslides (Pudasaini & Hutter 2007, Chap. 2.7.3) is to assume that the flowing regolith constitutes an incompressible continuum. This assumption rests upon several observations. Large terrestrial landslides have a nearly

https://doi.org/10.1017/jfm.2026.11369 Published online by Cambridge University Press

plug-like flow (Melosh 1986), so that shearing occurs only in a thin layer near the base. Consequently, the dilatation that accompanies granular flows is confined to a small region of the flow. Later, we will depth average our equations, so that ignoring these volume changes will not affect our results in a significant manner. The mass balance and linear momentum balance for an incompressible flow in the body-fixed coordinate system $\mathcal{E}_0$ are, respectively,

$$\nabla \cdot \boldsymbol{u} = 0 \quad \text{and} \quad \rho \frac{\partial \boldsymbol{u}}{\partial t} + \nabla \cdot (\rho \boldsymbol{u} \otimes \boldsymbol{u}) = \nabla \cdot \boldsymbol{\sigma} + \rho(\boldsymbol{b} - 2\boldsymbol{\omega} \times \boldsymbol{u} - \boldsymbol{r} \times \boldsymbol{\alpha} - \boldsymbol{A}_c), \quad (2.1)$$

where $\boldsymbol{u}$ is the flow's velocity relative to $\mathcal{E}_0$, ρ is the regolith's mean density, $\boldsymbol{\sigma}$ is the stress tensor, $\boldsymbol{\omega}$ and $\boldsymbol{\alpha}$ are, respectively, the central body's angular velocity and angular acceleration, $\boldsymbol{r}$ is a mass element's position vector relative to C, $\boldsymbol{b} = \boldsymbol{b}^0 - \boldsymbol{\omega} \times (\boldsymbol{\omega} \times \boldsymbol{r})$ is the total effective gravity in terms of the central body's gravity $\boldsymbol{b}^0$ and the centrifugal acceleration $\boldsymbol{\omega} \times (\boldsymbol{\omega} \times \boldsymbol{r})$, $2\boldsymbol{\omega} \times \boldsymbol{u}$ is the Coriolis acceleration and $\boldsymbol{A}_C$ is the inertial acceleration of the central body's centre of mass. To complete (2.1) we need to prescribe a rheology appropriate for the granular continuum that relates the stress tensor to the flow's strain rate, and we return to this in the next section.

Next, we consider how the central body's dynamics couples to the regolith flow. In the inertial coordinate system $\mathcal{P}$, the linear momentum balance of the system comprising of the central body and the flowing regolith is

$$\frac{\mathrm{d}}{\mathrm{d}t}(M_c \boldsymbol{U}_c) + \frac{\mathrm{d}}{\mathrm{d}t}(M_r \boldsymbol{U}_r) = \boldsymbol{F} - \boldsymbol{F}_s, \quad (2.2)$$

where the subscripts 'c' and 'r' indicate the central body and the flowing regolith, respectively, M is the mass, $\boldsymbol{U}$ is the centre of mass velocity, $\boldsymbol{F}$ represents external forces on the system and $\boldsymbol{F}_s$ is the rate of momentum carried away by the mass shed from the body's surface. Due to erosion and deposition during landsliding, mass is exchanged between the stationary regolith (central body) and the flowing grains, so that M_c and M_r may be modified. Additionally, M_r may also change due to surface mass shedding.

Finally, in the inertial coordinate system $\mathcal{P}$, the global angular momentum balance of the system about the point P is

$$\frac{\mathrm{d}\boldsymbol{H}_c}{\mathrm{d}t} + \frac{\mathrm{d}\boldsymbol{H}_r}{\mathrm{d}t} = \boldsymbol{T} - \boldsymbol{T}_s, \quad (2.3)$$

where the subscripts 'c' and 'r' are as above, $\boldsymbol{H}$ represents angular momentum, $\boldsymbol{T}$ is the external torque and $\boldsymbol{T}_s$ is the rate at which angular momentum is carried away by the shed mass. The above angular momentum balance is simplified further in Appendix A to obtain the following form:

$$\boldsymbol{\omega} \times (\boldsymbol{I} \cdot \boldsymbol{\omega} + \boldsymbol{h}_r) + \boldsymbol{I} \cdot \boldsymbol{\alpha} + \dot{\boldsymbol{h}}_r + \dot{\boldsymbol{I}} \cdot \boldsymbol{\omega} + \boldsymbol{R}_O \times M\boldsymbol{A}_c = \boldsymbol{T} - \boldsymbol{T}_s, \quad (2.4)$$

where $\boldsymbol{I}$ is the moment of inertia about C of the system comprised, in general, a static part (central body) and flowing regolith, $\boldsymbol{h}_r$ is the angular momentum of the flowing regolith about C in the body-fixed coordinate system $\mathcal{E}_0$, $\dot{(\,)}$ represents time differentiation in the body-fixed coordinate system and M and $\boldsymbol{R}_O$ are, respectively, the total system mass and the location of its centre of mass with respect to C. The first term on the left-hand side of (2.4) arises from the tumbling motion of the central body, the second is the rotational inertia and the third and fourth terms are due to regolith flow and the final term is because the centre of mass of the system may not be at the origin C, which introduces an extra contribution from the centre of mass's acceleration.

https://doi.org/10.1017/jfm.2026.11369 Published online by Cambridge University Press

Thus far, while developing our modelling framework, we have made no assumptions regarding forces and torques affecting our system, nor have we imposed any constraints on the kinematics of the central body or the nature of landslides. We may, in principle, implement this framework computationally. However, in the next section we introduce several physically motivated simplifications that make the presentation accessible, without sacrificing essential details or negating practical application.

Two remarks are in order before we close this section. First, when landslides occur the body consists of a solid central body and a flowing regolith layer. Thus, we cannot strictly ascribe to the body an angular velocity, at least in the sense of a rigid body. However, landsliding events are intermittent, with each landslide remaining active for a duration of time much shorter than the rotational dynamics time scale and, moreover, landslides are typically of depth much smaller in comparison with the body's size. Thus, we may identify the central body's rotational motion with that of the body itself. Second, as mentioned, we believe that landslides are most commonly initiated by seismic activity following an impact event. Here, we will not concern ourselves with how the location and amount of mobilised regolith is related to the details of the corresponding impact. Instead, in the sections to follow we will make simplifying assumptions and leave detailed modelling of this aspect to future work. This is done to retain focus in this work on how landslides affect, and are affected by, the shape and rotational motion of small rubble planetary bodies.

3. A simplified model

Figure 1 shows asteroids Bennu and Ryugu that were the targets of recent missions. Their shapes are observed to be fairly axisymmetric and the objects were found to be in pure spin about the symmetry axis. This suggests specialising our model to an axisymmetric situation, wherein the initial body and all subsequent landslides are axisymmetric about a space-fixed rotation axis. We further assume that the landslides are shallow, in that their depth normal to the body's topography is much smaller than the extent of their spread over the body's surface. Consequently, the momentum carried by the regolith flow and shed mass is much smaller than the system's orbital momentum, which then balances the Sun's gravitational force on the right in (2.2). The angular acceleration arising from landslide-induced changes in the body's moment of inertia is nevertheless retained. This is because, for a spherical shell of thickness H and diameter D, the mass scales as D^2H, whereas the moment of inertia scales as D^4H. Indeed, Banik *et al.* (2022) found that, although the change in the body's rotation due to each landslide over its lifetime is small, the cumulative effect is significant. This is similar to the action of radiation torques discussed below, and makes the case for the present modelling that couples these torques with landsliding.

Now, the external forces ($\boldsymbol{F}$) and moments ($\boldsymbol{T}$) entering into the governing (2.2) and (2.4) arise from gravitational attraction of the Sun and other bodies, (thermal) radiation pressure and radiation torques. Radiation pressure – the Yarkovsky effect – influences orbital motion, while radiation torques – also called YORP torques, or simply YORP – change the body's rotation, especially over long time periods; please see Vokrouhlický *et al.* (2015) for more information. Here, we limit ourselves to small isolated objects. Thus, the Sun's quadrupole torque – torque due to varying Solar gravitational forces experienced at different parts of the body – is negligible, as are tidal interactions. Furthermore, the orbital drift of sub-kilometre-sized asteroids caused by the Yarkovsky effect is typically of the order of $10^{-4}-10^{-3}$ AU/Myr, where AU is the astronomical unit and Myr represents a million years (Vokrouhlickỳ *et al.* 2000). Therefore, the orbital change – and consequently its influence on the YORP torque – may be neglected when simulating over a time scale of a few million years. Along with our assumption above regarding the balance of orbital

https://doi.org/10.1017/jfm.2026.11369 Published online by Cambridge University Press

inertia and the Sun's gravitational force in (2.2), these considerations decouple the angular momentum balance (2.4) from (2.2). Thus, we may study landslides independently of the body's orbital motion and external gravity forces.

The angular momentum balance (2.4) is further simplified for bodies that are nominally in a state of pure spin, i.e. bodies with a space-fixed rotation axis $\hat{\boldsymbol{e}}_3$, which is generally their axis of greatest moment of inertia. This is true for many small planetary objects, including the asteroids in figure 1. As mentioned in the introduction, internal friction damps out tumbling motion in bodies in free space, driving them into a state of pure spin about their axis of greatest inertia (Burns *et al.* 1973; Sharma *et al.* 2005; Breiter *et al.* 2012).

For a body in pure spin about $\hat{\boldsymbol{e}}_3$ we have $\boldsymbol{\omega} = \omega\hat{\boldsymbol{e}}_3$ and $\boldsymbol{\alpha} = \alpha\hat{\boldsymbol{e}}_3$. Invoking this and the simplifications above, we arrive at the following coupled equations for shallow, incompressible regolith flow on a planetary body in pure spin:

$$\boldsymbol{\nabla}\cdot\boldsymbol{u} = 0, \tag{3.1}$$

$$\rho\dot{\boldsymbol{u}} + \boldsymbol{\nabla}\cdot(\rho\boldsymbol{u}\otimes\boldsymbol{u}) = \boldsymbol{\nabla}\cdot\boldsymbol{\sigma} + \rho(\boldsymbol{b} - 2\boldsymbol{\omega}\times\boldsymbol{u} - \boldsymbol{\alpha}\times\boldsymbol{r}), \tag{3.2}$$

and

$$I\alpha + \dot{h}_r + \dot{I}\omega = T - T_s, \tag{3.3}$$

where I and h_r are, respectively, the system's moment of inertia and the flowing regolith's angular momentum about the rotation axis $\hat{\boldsymbol{e}}_3$ and $T - T_s = (\boldsymbol{T} - \boldsymbol{T}_s)\cdot\hat{\boldsymbol{e}}_3$. We recall that the system here consists of the central body and, when applicable, the flowing regolith. Note also that the angular momentum balance reduces to the scalar equation above when we take the body to be in a state of pure spin.

We also require a rheology of the flowing regolith and boundary conditions (BCs) to close the set (3.1) and (3.2). We introduce the former in § 3.3 below, but discuss the latter now. At the free top surface $F^s(\boldsymbol{r}) = 0$ of the flow, identified by the superscript s, we impose the vanishing of the traction and the usual kinematic conditions, respectively,

$$\boldsymbol{\sigma}^s\cdot\boldsymbol{n}^s = 0, \tag{3.4a}$$

and

$$\frac{\partial F^s}{\partial t} + (\boldsymbol{u}\cdot\boldsymbol{\nabla})\,F^s = 0, \tag{3.4b}$$

where $\boldsymbol{n}^s$ is the normal to the free surface.

We assume no erosion of material from the central body during a landslide, i.e. mass is not added from the central body to the flowing regolith across the flow's base. This is a simplifying but not limiting assumption, and may be relaxed in the future. The flow adheres to the basal topography and the surface traction there is assumed to be governed by Coulomb's friction law. The mathematical statements of these BCs at the flow's base are, respectively,

$$\boldsymbol{u}^b\cdot\boldsymbol{n}^b = 0, \tag{3.5a}$$

and

$$\left(\boldsymbol{1} - \boldsymbol{n}^b\otimes\boldsymbol{n}^b\right)\cdot\boldsymbol{\sigma}^b\cdot\boldsymbol{n}^b = -\mu\boldsymbol{n}^b\cdot\boldsymbol{\sigma}^b\cdot\boldsymbol{n}^b\frac{\boldsymbol{u}^b}{|\boldsymbol{u}^b|}, \tag{3.5b}$$

where μ is the basal friction coefficient. Landslides flow over the central body, which comprises the same type of grains, so that we set $\tan^{-1}\mu = \zeta$, the regolith's internal friction angle. Note that (3.5*a*) is equivalent to the usual no-penetration condition. Finally,

https://doi.org/10.1017/jfm.2026.11369 Published online by Cambridge University Press

mass shedding is assumed to commence when the pressure at the flow's base, denoted by the superscript b, becomes tensile in nature, i.e. when

$$\boldsymbol{n}^b \cdot \boldsymbol{\sigma}^b \cdot \boldsymbol{n}^b > 0. \tag{3.6}$$

This criterion is analogous to that employed by Scheeres (2015) and Sánchez & Scheeres (2020), except that they consider the loss of a single grain from the body's surface, which happens when the normal reaction vanishes.

Now, limiting ourselves to shallow axisymmetric landslides on an initially axisymmetric body allows us to reduce the spatial dimensionality of the governing equations to one, because derivatives in the longitudinal direction vanish and we may depth average our equations in a direction normal to the base. The latter is equivalent to ignoring variations in the regolith flow across its depth. Furthermore, because the regolith flow's thickness is much smaller compared with the central body's mean radius R_{CB}, we may now introduce the small parameter

$$\varepsilon = H/R_{CB} \ll 1, \tag{3.7}$$

where H is the average thickness of the flow when it is initiated. This allows us to approximate various quantities by ignoring variations that are $\mathcal{O}(\varepsilon)$ or smaller. These steps simplify our mathematical description considerably, as we now see.

3.1. *Axisymmetric coordinate system*

We will now depth integrate the linear momentum balance (3.2) in a manner similar to Gray *et al.* (1999) and Luca *et al.* (2016). To facilitate this we first introduce the natural axisymmetric coordinate system associated with the body's shape; see, for example, the schematic in figure 2(*b*). We will express our governing equations in this coordinate system.

The central body's axisymmetric surface is defined by its distance $r_{CB} = R(\theta)$ from C in terms of the co-latitude θ. To describe the regolith flow over the central body's surface, we introduce the contravariant coordinate system $(x^1, x^2, x^3) = (n, \theta, \phi)$, where n is the normal distance from the central body's surface and ϕ is the longitude. A material point within the regolith flow is then located by

$$\boldsymbol{r} = r_{CB}\hat{\boldsymbol{e}}_r + n\hat{\boldsymbol{n}} = R(\theta)\hat{\boldsymbol{e}}_r + n\hat{\boldsymbol{n}}, \tag{3.8a}$$

where

$$\hat{\boldsymbol{n}} = \left(R\hat{\boldsymbol{e}}_r - R'\hat{\boldsymbol{e}}_\theta\right)N^{-1}, \tag{3.8b}$$

is the outward unit surface normal, $N = \sqrt{R^2 + R'^2}$, $\hat{\boldsymbol{e}}_i$ are the unit vectors in spherical coordinates and prime $(\prime)$ denotes differentiation with respect to θ.

The natural basis vectors $\boldsymbol{g}_i$ are obtained as $\boldsymbol{g}_i = \partial \boldsymbol{r}/\partial x^i$

$$\boldsymbol{g}_1 = \hat{\boldsymbol{n}}, \qquad \boldsymbol{g}_2 = \frac{\kappa_\theta^b}{\kappa_\theta}(R'\hat{\boldsymbol{e}}_r + R\hat{\boldsymbol{e}}_\theta) \quad \text{and} \quad \boldsymbol{g}_3 = \frac{\hat{\boldsymbol{e}}_\phi}{\kappa_\phi}, \tag{3.9}$$

where κ_θ and $\kappa_\phi = \sqrt{\kappa_{\phi n}^2 + \kappa_{\phi g}^2}$ are the curvatures of $\theta-$ and $\phi-$ coordinate curves, with $\kappa_{\phi g}$ and $\kappa_{\phi n}$ being, respectively, the geodesic and normal curvatures of the ϕ-curves, and the superscript b indicates that the quantity is evaluated at the central body's surface. The formulae for these curvatures are

$$\kappa_\theta^b = \frac{R^2 + 2R'^2 - RR''}{N^3}, \quad \kappa_\phi^b = \frac{1}{R\sin\theta}, \quad \kappa_\theta = \frac{\kappa_\theta^b}{1 + \kappa_\theta^b n} \quad \text{and} \quad \kappa_\phi = \frac{\kappa_\phi^b}{1 + \kappa_{\phi n}^b n}, \tag{3.10}$$

https://doi.org/10.1017/jfm.2026.11369 Published online by Cambridge University Press

and

$$\kappa^b_{\phi n} = -\frac{(R\cos\theta)'}{NR\sin\theta}, \quad \kappa^b_{\phi g} = \frac{(R\sin\theta)'}{NR\sin\theta}, \quad \kappa_{\phi n} = \frac{\kappa^b_{\phi n}}{1+\kappa^b_{\phi n} n} \quad \text{and} \quad \kappa_{\phi g} = \frac{\kappa^b_{\phi g}}{1+\kappa^b_{\phi n} n}. \tag{3.11}$$

Finally, the radius of curvature for the θ- and ϕ-curves are, respectively,

$$\mathcal{R}_\theta = 1/\kappa_\theta \quad \text{and} \quad \mathcal{R}_\phi = 1/\kappa_\phi. \tag{3.12}$$

The basis vectors $\boldsymbol{g}_i$ calculated in (3.9) are orthogonal. In such bases, employing index notation where possible, the divergence of vector ($\boldsymbol{v}$) and tensor ($\boldsymbol{T}$) fields have the compact representations

$$\boldsymbol{\nabla}\cdot\boldsymbol{v} = \sum_{i=1}^{3} \frac{1}{g}\frac{\partial}{\partial x^i}\left(\frac{v_i\, g}{\sqrt{g_{ii}}}\right), \tag{3.13}$$

and

$$\boldsymbol{\nabla}\cdot\boldsymbol{T} = \sum_{i,j=1}^{3} \sqrt{g_{ii}}\left(\frac{1}{g}\frac{\partial}{\partial x^j}\left(\frac{g T_{ji}}{\sqrt{g_{ii}}\sqrt{g_{jj}}}\right) + \sum_{k=1}^{3}\Gamma^i_{jk}\frac{T_{kj}}{\sqrt{g_{jj}}\sqrt{g_{kk}}}\right)\hat{\boldsymbol{g}}_i, \tag{3.14}$$

where $g_{ij} = \boldsymbol{g}_i\cdot\boldsymbol{g}_j$ is the metric tensor, $g = \sqrt{\det[g_{ij}]}$ (no sum) is its norm, $\hat{\boldsymbol{g}}_i = \boldsymbol{g}_i/\sqrt{g_{ii}}$ (no sum) are unit vectors, $v_i = \boldsymbol{v}\cdot\hat{\boldsymbol{g}}_i$ and $T_{ij} = \hat{\boldsymbol{g}}_i\cdot\boldsymbol{T}\cdot\hat{\boldsymbol{g}}_j$ are the covariant components of the vector and tensor fields, respectively, and $\Gamma^i_{jk} = \boldsymbol{g}^i\cdot(\partial\boldsymbol{g}_j/\partial x^k)$ are the Christoffel symbols. For our coordinate system we obtain

$$g_{11} = 1, \quad g_{22} = \left(\frac{\kappa^b_\theta}{\kappa_\theta}N\right)^2, \quad g_{33} = \frac{1}{\kappa^2_\phi}, \quad g_{ij} = 0 \;\forall\; i\neq j, \quad g = \frac{N\kappa^b_\theta}{\kappa_\theta\kappa_\phi} \quad \text{and} \quad J = g, \tag{3.15}$$

where J is the Jacobian of the transformation from Cartesian to the axisymmetric coordinate system.

3.2. *Non-dimensionalisation*

Before proceeding, we non-dimensionalise our equations as per the following definitions:

$$\begin{gathered}\{n,t\} = \left\{Hn^*, \sqrt{R_{CB}/b}\,t^*\right\}; \qquad \left\{u_n, u_\theta, u_\phi\right\} = \sqrt{bR_{CB}}\left\{\varepsilon u_n^*, u_\theta^*, u_\phi^*\right\}; \\ \{\omega, T\} = \left\{\sqrt{b/R_{CB}}\,\omega^*, \rho b R^4_{CB}\,T^*\right\}; \quad \text{and} \quad \sigma_{ij} = \rho b H\,\sigma^*_{ij},\end{gathered} \tag{3.16}$$

where H is the initial average thickness of the landslide, b is the gravitational acceleration on the surface of a sphere of radius R_{CB} and superscript * identifies non-dimensional quantities; the * is subsequently dropped for a cleaner notation.

https://doi.org/10.1017/jfm.2026.11369 Published online by Cambridge University Press

3.2.1. *Governing equations*

The continuity and linear momentum balance equations, upon using (3.9)–(3.16) and assuming axisymmetry, simplify to, respectively,

$$\frac{\partial}{\partial n}\left(Ju_n\right)+\frac{\partial}{\partial \theta}\left(\mathcal{R}_\phi u_\theta\right)=0, \tag{3.17}$$

$$\varepsilon\frac{\partial}{\partial t}\left(Ju_n\right)+\frac{\partial}{\partial n}\left(JA_{nn}\right)+\varepsilon\frac{\partial}{\partial \theta}\left(\mathcal{R}_\phi A_{n\theta}\right)=J\left(\kappa_\theta A_{\theta\theta}+\kappa_{\phi n}A_{\phi\phi}+f_n\right), \tag{3.18}$$

$$\frac{\partial}{\partial t}\left(J^2\kappa_\phi u_\theta\right)+\frac{\partial}{\partial n}\left(J^2\kappa_\phi A_{n\theta}\right)+\frac{\partial}{\partial \theta}\left(JA_{\theta\theta}\right)=\frac{\partial}{\partial \theta}\left(J\kappa_\phi\right)\mathcal{R}_\phi A_{\theta\theta}\ \ldots$$
$$\ldots+J^2\kappa_\phi\left(\kappa_{\phi g}A_{\phi\phi}+f_\theta\right) \tag{3.19}$$

and

$$\frac{\partial}{\partial t}\left(J\mathcal{R}_\phi u_\phi\right)+\frac{\partial}{\partial n}\left(J\mathcal{R}_\phi A_{n\phi}\right)+\frac{\partial}{\partial \theta}\left(\mathcal{R}_\phi^2 A_{\theta\phi}\right)=J\mathcal{R}_\phi f_\phi, \tag{3.20}$$

where

$$A_{nn}=\varepsilon u_n^2-\sigma_{nn},\quad A_{ni}=u_nu_i-\sigma_{ni}\ \text{ and }\ A_{ij}=u_iu_j-\varepsilon\sigma_{ij}, \tag{3.21}$$

with i and j representing either θ or ϕ and where f_i are the body force terms

$$f_n=b_n^0+\mathcal{R}_\phi\kappa_{\phi n}\left(\mathcal{R}_\phi\omega^2+2\omega u_\phi\right), \tag{3.22a}$$

$$f_\theta=b_\theta^0+\mathcal{R}_\phi\kappa_{\phi g}\left(\mathcal{R}_\phi\omega^2+2\omega u_\phi\right) \tag{3.22b}$$

and

$$f_\phi=-\mathcal{R}_\phi\left(2\omega(\varepsilon\kappa_{\phi n}u_n+\kappa_{\phi g}u_\theta)+\alpha\right), \tag{3.22c}$$

in terms of $b_n^0=\boldsymbol{b}^0\cdot\hat{\boldsymbol{g}}_1$ and $b_\theta^0=\boldsymbol{b}^0\cdot\hat{\boldsymbol{g}}_2$.

3.2.2. *Boundary conditions*

The non-dimensionalised kinematic BC at the top and bottom surfaces are given by, respectively,

$$J^su_n^s-\frac{u_\theta^s}{\kappa_\phi^s}\frac{\partial h}{\partial \theta}=J^s\frac{\partial h}{\partial t} \tag{3.23a}$$

and

$$u_n^b=0, \tag{3.23b}$$

where s and b represents top and bottom surfaces. The normal to the top surface is

$$\boldsymbol{n}^s=\frac{\boldsymbol{\nabla}F}{|\boldsymbol{\nabla}F|}=\left[J^2+\left(\mathcal{R}_\phi\frac{\partial h}{\partial \theta}\right)^2\right]^{-\frac{1}{2}}\left(J\hat{\boldsymbol{g}}_1-\mathcal{R}_\phi\frac{\partial h}{\partial \theta}\hat{\boldsymbol{g}}_2\right). \tag{3.24}$$

Employing (3.24), we obtain the non-dimensionalised dynamic BCs at the top surface as

$$\sigma_{nn}^s-\varepsilon\frac{\sigma_{n\theta}^s}{J^s\kappa_\phi^s}\frac{\partial h}{\partial \theta}=0, \tag{3.25a}$$

$$\sigma_{n\theta}^s-\varepsilon\frac{\sigma_{\theta\theta}^s}{J^s\kappa_\phi^s}\frac{\partial h}{\partial \theta}=0 \tag{3.25b}$$

https://doi.org/10.1017/jfm.2026.11369 Published online by Cambridge University Press

and

$$\sigma^s_{n\phi} - \varepsilon \frac{\sigma^s_{\theta\phi}}{J^s \kappa^s_\phi} \frac{\partial h}{\partial \theta} = 0. \tag{3.25c}$$

At the bottom surface, with i representing either θ or ϕ, we have

$$\sigma^b_{ni} = -\mu \hat{u}^b_i \sigma^b_{nn}, \tag{3.26a}$$

where, we have introduced the scaled velocity

$$\hat{u}^b_i = \frac{u^b_i}{\sqrt{(u^b_\theta)^2 + (u^b_\phi)^2}}. \tag{3.26b}$$

3.3. *Depth averaging*

We now define the depth-averaged quantities, identified by $\bar{(\cdot)}$

$$\{\overline{v}(\theta, t), \overline{w}(\theta, t)\} = \frac{1}{h} \int_0^h \{v(n, \theta, t), w(n, \theta, t)\} \, \mathrm{d}n \tag{3.27a}$$

and

$$\overline{vw} = \beta_{vw}(\theta, t) \overline{v}\, \overline{w}, \tag{3.27b}$$

where h is the flow's depth scaled by its initial average thickness H and the depth-variation parameter β_{vw} is introduced to express the average of the product of velocities as the product of their individual averages. A plug-like velocity profile is a fairly good assumption for granular flows (Melosh 1986; Pudasaini & Hutter 2007). Consequently, we approximate β_{vw} as unity, as did Gray *et al.* (1999). This allows us to equate the depth-averaged velocity to the basal velocity, i.e.

$$\bar{\boldsymbol{u}} = \boldsymbol{u}^b. \tag{3.28}$$

To close our mathematical description, we need a rheological description of the shallow regolith flow. We express the stress tensor as

$$\boldsymbol{\sigma} = -p\mathbf{1} + \boldsymbol{\tau}, \tag{3.29}$$

where p is the pressure and $\boldsymbol{\tau}$ is the deviatoric stress tensor. Gray & Edwards (2014) and Baker, Barker & Gray (2016) proposed a depth-averaged constitutive law of the form

$$h\bar{\boldsymbol{\tau}} = \rho \nu h^{3/2} \bar{\boldsymbol{D}}, \tag{3.30}$$

where ν and $\bar{\boldsymbol{D}}$ are the depth-averaged viscosity and two-dimensional strain rate tensor, respectively. The depth-averaged viscosity ν may be expressed in terms of material parameters and slope of the basal surface; see Baker *et al.* (2016, (2.27)). However, the contribution from $\bar{\boldsymbol{\tau}}$ in the depth-averaged linear momentum balance is generally rather small (Baker *et al.* 2016; Rocha, Johnson & Gray 2019). Given this, for simplicity, here we ignore $\bar{\boldsymbol{\tau}}$ and set

$$\overline{\sigma}_{\theta\theta} = \overline{\sigma}_{\phi\phi} = \overline{\sigma}_{nn} = -\overline{p}. \tag{3.31}$$

This is consistent with the observation (Melosh 1986) that downslope granular flows are plug-like, with shearing confined near the base, so that shear stresses are generally small through the flow's depth. The only resistance to the flow is thus from basal friction.

We now list some further approximations that we make while depth averaging. The curvatures may be written as $\kappa_i = \kappa^b_i + O(\varepsilon)$, because we assume curvatures to be of $O(1/R_{CB})$. Therefore, we set curvatures to be constant while depth averaging, which

https://doi.org/10.1017/jfm.2026.11369 Published online by Cambridge University Press

introduces an error of $O(\varepsilon)$. We also neglect the contribution of Coriolis force arising from the normal component u_n of the flow velocity, as it is also of $O(\varepsilon)$. Considering only the partial contribution from the Coriolis term is termed as the traditional approximation in the geophysical literature (Eckart 1960; Gerkema *et al.* 2008). We introduce the above approximations in the sections below. However, for completeness, in Appendix B we provide equations for regolith flow that include the constitutive law (3.30), the effect of curvature variations and which do not make the traditional approximation.

The depth-averaged momentum equation in the n-direction now becomes

$$p = \psi(h - n) + O(\varepsilon), \tag{3.32a}$$

where

$$\psi = -(f_n + \kappa_\theta \bar{u}_\theta^2 + \kappa_{\phi n} \bar{u}_\phi^2) \tag{3.32b}$$

is defined in terms of the body force term

$$f_n = b_n^0 + \mathcal{R}_\phi \kappa_{\phi n} \big(\mathcal{R}_\phi \omega^2 + 2\omega \bar{u}_\phi\big). \tag{3.32c}$$

The form (3.32*a*) and (3.32*b*) of the pressure field is similar to the one obtained by employing the quasi-hydrostatic approximation in geophysical fluid dynamics (White *et al.* 2005). In (3.32*b*) and (3.32*c*), we note the presence of contributions of centripetal acceleration through terms quadratic in velocity components u_θ and u_ϕ and angular velocity ω. Coriolis acceleration results in the last term in f_n. While centripetal terms always lower the basal pressure p, the Coriolis effect may raise or lower p depending upon the signs of ω, the curvature $\kappa_{\phi n}$ and the azimuthal velocity $\bar{u}_\phi$. As mentioned, mass shedding commences when basal pressure becomes negative which, from (3.32*a*), is equivalent to the requirement that

$$\psi < 0. \tag{3.33}$$

Incorporating the above, our final depth-averaged continuity and linear momentum balance equations governing shallow regolith flow when mass shedding is absent, i.e. $\psi > 0$, become, respectively,

$$\frac{\partial}{\partial t}(Jh) + \frac{\partial}{\partial \theta}\left(\mathcal{R}_\phi \bar{u}_\theta h\right) = 0, \tag{3.34}$$

$$\frac{\partial}{\partial t}(J\bar{u}_\theta h) + \frac{\partial}{\partial \theta}\left\{\left(\bar{u}_\theta^2 + \frac{\varepsilon}{2}\psi h\right)\mathcal{R}_\phi h\right\} = \left[-\mu\psi\hat{\bar{u}}_\theta + b_\theta^0 + \kappa_{\phi g}\left\{\bar{U}_\phi^2 + \varepsilon\psi\frac{h}{2}\right\}\right]Jh \tag{3.35}$$

and

$$\frac{\partial}{\partial t}\left(J\mathcal{R}_\phi \bar{U}_\phi h\right) + \frac{\partial}{\partial \theta}\left(\mathcal{R}_\phi^2 \bar{u}_\theta \bar{U}_\phi h\right) = -\mu J \mathcal{R}_\phi \psi \hat{\bar{u}}_\phi h, \tag{3.36}$$

where $\hat{\bar{u}}_\theta$ and $\hat{\bar{u}}_\phi$ are defined as in (3.26*b*) and

$$\bar{U}_\phi = \bar{u}_\phi + \mathcal{R}_\phi \omega \tag{3.37}$$

is the regolith's azimuthal velocity in the inertial frame. The equations above have to be solved for the flow rate $\{\bar{u}_\theta, \bar{u}_\phi\}$ and depth h of the landslide. Finally, mass is shed from regions where $\psi < 0$. In those regions, because we employ a depth-averaged formulation, mass shedding necessarily implies that material across the full flow depth is removed. Thus, we set

$$h = \bar{u}_\theta = \bar{u}_\phi = 0. \tag{3.38}$$

https://doi.org/10.1017/jfm.2026.11369 Published online by Cambridge University Press

In Appendix D we provide details of how we have validated our landslide model above.

We now make two remarks regarding the regolith's total energy and the angular momentum. First, the energy in this system is dissipated only due to basal sliding. Indeed, the energy equation is shown in Appendix C to be

$$\frac{\partial}{\partial t}\left\{Jh\left(\frac{|\bar{U}|^2}{2}+V(\theta)-\varepsilon b_n^0\frac{h}{2}\right)\right\}+\frac{\partial}{\partial\theta}\left\{\left(\frac{|\bar{U}|^2}{2}+V(\theta)-\varepsilon b_n^0 h\right)\mathcal{R}_\phi\bar{u}_\theta h\right\} = -\mu J\psi h\left(|\bar{u}|+\mathcal{R}_\phi\omega\hat{\bar{u}}_\phi\right)+O(\varepsilon), \tag{3.39}$$

where $|\bar{U}|^2=\sqrt{\bar{U}_\theta^2+\bar{U}_\phi^2}$, $|\bar{u}|^2=\sqrt{\bar{u}_\theta^2+\bar{u}_\phi^2}$ and $V(\theta)$ is the gravitational potential at the surface the of central body, so that

$$b_\theta^0=-\frac{\mathcal{R}_\phi}{J}\frac{\partial V}{\partial\theta}. \tag{3.40}$$

In the next section we show that (3.36) represents the angular momentum balance of a ring-shaped volume element $\mathrm{d}V$ of the axisymmetric regolith flow – sketched in brown in figure 2(*a*). Thus, (3.36) reveals that the angular momentum of this ring element is advected across latitudes by the velocity $\bar{u}_\theta$ and exchanged with the central body by basal friction.

3.4. *Rotational dynamics*

It remains to follow the evolution of the body's rotation rate ω. The angular momentum balance (3.3) after non-dimensionalisation and invoking axisymmetry becomes

$$\alpha=\left\{T-2\pi\varepsilon\int_{\psi\geq0}J\mathcal{R}_\phi\frac{\partial}{\partial t}\left(h\bar{U}_\phi\right)\,\mathrm{d}\theta\right\}I_c^{-1}+O(\varepsilon^2), \tag{3.41a}$$

where

$$I_c=2\pi\int_0^\pi\frac{1}{5}\mathcal{R}_\phi^3R^2\,\mathrm{d}\theta \tag{3.41b}$$

is the central body's moment of inertia about symmetry axis. The integral in (3.41*a*) is over those regions where the basal pressure does not vanish, i.e. $\psi\geqslant0$. We find that the term inside the integral in (3.41*a*) is exactly the first term in (3.36) which may, hence, be interpreted as the angular momentum balance for the ring-shaped granular element $\mathrm{d}V$ in figure 2(*a*). We note that employing (3.36) we may also write the expression for angular acceleration in the simpler form

$$\alpha=I_c^{-1}\left\{T+2\pi\varepsilon\int_{\psi\geq0}\mu J\mathcal{R}_\phi\psi\hat{\bar{u}}_\phi h\,\mathrm{d}\theta\right\}+O(\varepsilon^2). \tag{3.42}$$

From (3.41*a*) or (3.42) we may determine the angular acceleration α at any time in terms of the average azimuthal velocity $\bar{u}_\phi$ and the depth h of the landslide. Time integration of α yields ω as a function of time.

4. Applications

We now investigate two different applications in turn.

https://doi.org/10.1017/jfm.2026.11369 Published online by Cambridge University Press

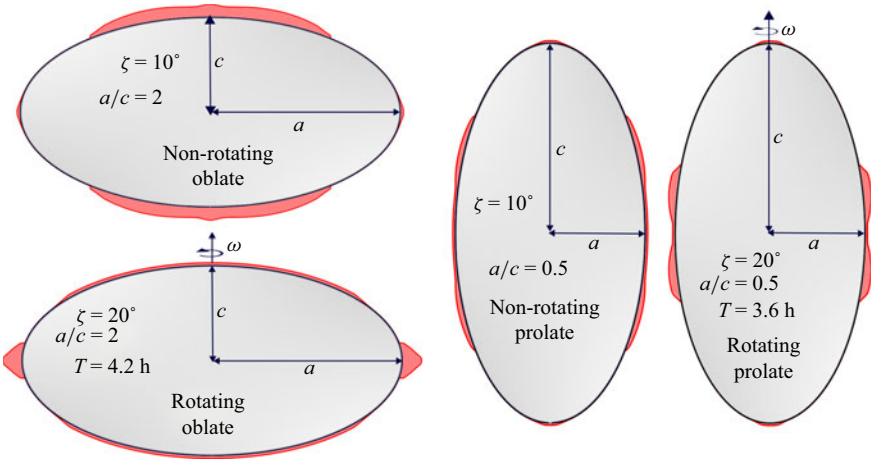


Figure 3. Final regolith deposited by landsliding of an initially uniform regolith layer on stationary and rotating oblate and prolate ellipsoids. The regolith height is magnified two times for clarity.

4.1. *Isolated landslides*

We investigate regolith flows on rotating bodies in two limits, *viz.* the rotation rate being zero and very fast. This is done to understand gravity- and rotation-driven flows, respectively.

We initiate the flow by distributing regolith uniformly over the body's surface with depth $H = \varepsilon R_{CB}$, where we arbitrarily set $\varepsilon = 0.01$. Thus, the initial conditions are

$$\text{at} \quad t = 0: \qquad h = 1 \quad \text{and} \quad \bar{u}_\theta = \bar{u}_\phi = 0 \quad \text{for all} \quad \theta \in (0, \pi), \tag{4.1}$$

where h is the flow's scaled depth. The flow of the ensuing landslide is then found by numerically solving (3.34)–(3.36) utilising the non-oscillatory central schemes of Kurganov & Tadmor (2000). The gravity field of the axisymmetric body is found by slicing the body into infinitesimal discs along the symmetry axis and then adding their individual contributions (Huré 2012).

Figure 3 presents the final deposition profile of an initially uniformly distributed regolith layer on an oblate and a prolate body that were either stationary or rotating fast. When rotation is absent, the gravitational field is too weak to overcome the basal resistance that keeps the regolith immobile; thus results are shown for a small friction angle $\zeta = 10°$. We find that landslides transport grains to the poles on an oblate body and to the equator for a prolate body when they are not rotating. This is because the tangential component of the gravity is always towards the poles for an oblate body, but towards the equator for a prolate body. In contrast, rotational effects always drive grains to the equator, as the tangential component of the centrifugal force along the body's surface is always directed towards the equator. Thus, for a prolate body, rotation assists the gravity-driven motion augmenting grain accumulation at the equator. On an oblate body, rotation and gravity compete, and we may find a comparable amount of regolith at both poles and the equator. We remark that rotation about the long axis of a prolate body is generally unstable. Thus, that example may be treated as illustrative.

We consider now applications to small planetary objects. For this we create axisymmetric bodies from shape models of actual, nominally axisymmetric, asteroids, such as Bennu and Ryugu from figure 1, and Itokawa. This is done by averaging the surface profiles of these bodies across longitudes at a fixed latitude.

https://doi.org/10.1017/jfm.2026.11369 Published online by Cambridge University Press

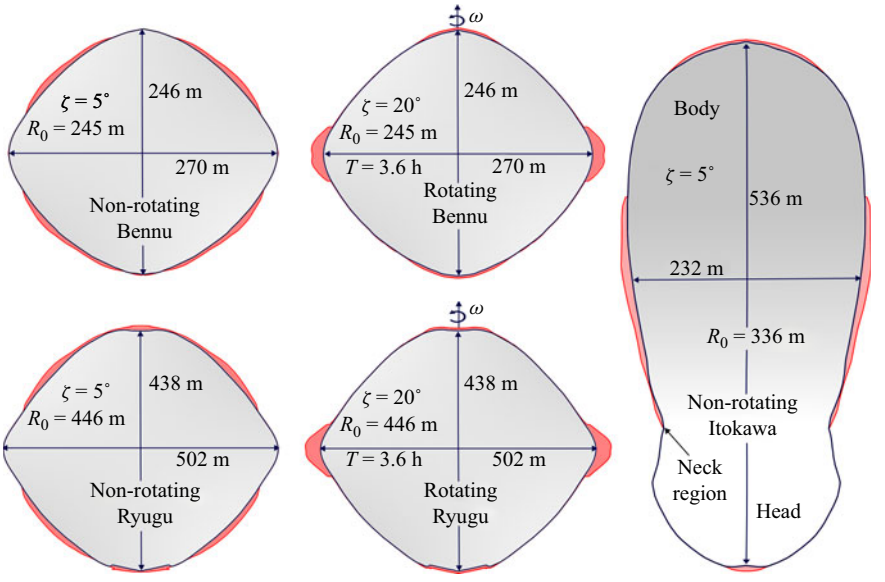


Figure 4. Final regolith deposited by landsliding of an initially uniform regolith layer on axisymmetrically modelled asteroids Bennu, Ryugu and Itokawa. The regolith thickness is magnified two times for clarity.

Figure 4 shows final deposits of initially uniformly spread regolith on asteroids Bennu, Ryugu and Itokawa. Were Bennu and Ryugu not rotating, then we would find grains accumulated at mid-latitudes. This is because the equilibria at the surface of such top-shaped bodies are located at their mid-latitudes (Banik *et al.* 2022). Interestingly, we find grains deposited around the poles of Ryugu due to the presence of a local topographical depression. These are the remnants of the initially placed regolith layer. Because the tangential component of both centrifugal and gravitational force is weak at the poles, the grains in their vicinity did not move away. New grains are not transported to the poles. At a higher rotation rate, we find that regolith accumulates at the equator, as in the examples in figure 3.

Finally, while Itokawa may be somewhat crudely approximated as an axisymmetric body, it is observed to rotate very slowly with a time period of 12 h about its short axis. Thus, to fit into our modelling we here investigate landsliding on a non-rotating Itokawa. We find that, while regolith migrates towards Itokawa's poles, a significant fraction is captured in the depression around the 'neck' region where Itokawa's 'head' and 'body' are joined.

4.2. *Shape and spin evolution of rubble piles*

We now explore two instances of the evolution of the shape and spin state of an initially spherical rubble asteroid over its lifetime due to impact-induced landsliding and the action of YORP torque. Before doing that we discuss in some detail the parameters we employ in our simulation, the manner in which they are chosen and how initial conditions are specified.

4.2.1. *Simulation details*

As already mentioned in the introduction and at the end of § 2, we do not model the impact process here. We simply assume that over time the asteroid experiences a fraction of impacts that are energetic enough to bring about global landsliding. Given the time t_s over

https://doi.org/10.1017/jfm.2026.11369 Published online by Cambridge University Press

Diameter	500 m
Density	1250 kg/m^3
Friction angle post-seismic shaking	30°
Friction angle during seismic shaking	10°
Seismic shaking duration	1 h
Failure thickness	1.875 m
YORP acceleration	0.83×10^{-6} degrees/day^2
Impact frequency	14.3 Myr^{-1}

Table 1. Parameters used for the simulations.

which we wish to investigate the asteroid's evolution, we follow the procedure of Banik *et al.* (2022) to calculate the number of such energetic impact events. We first estimate the minimum size d_{min} of the impactor that may cause global landslides (Richardson *et al.* 2005). We then compute the number of impactors with size bigger than d_{min} during time t_s (Holsapple 2022). These impacts may occur stochastically over a time scale t_s, but here we report results corresponding to a uniform temporal distribution. We then integrate the equations of motion, employing the parameters listed in table 1. Whenever an impact happens, we initiate a landslide by instantaneously mobilising a constant thickness of layer spread over the body. The thickness of the mobilised regolith is set in the manner of Banik *et al.* (2022), who took a thickness-to-slant-height ratio of $\varepsilon_{ls} = 0.005$ for a top-shaped asteroid. For our case, this corresponds to a thickness-to-radius ratio of $\varepsilon = 0.0075$. The initial condition for the regolith flow are thus given by

$$\text{at} \quad t = 0: \qquad h = 1, \quad \bar{u}_\theta = \bar{u}_\phi = 0 \quad \text{for all} \quad \theta \in (0, \pi) \quad \text{and} \quad \omega = \omega_0, \tag{4.2}$$

where ω_0 is the primordial rotation rate of the body.

When an impact mobilises a landslide, we lower the basal friction angle to incorporate the effects of post-impact seismic reverberations. This is similar to acoustic fluidisation in large landslides (Melosh 1986). We set the basal friction angle to 10° during the time over which seismic shaking persists, following the Luca *et al.* (2016) estimate. The basal frictional angle recovers to its original value of 30° once seismic shaking ceases; note that 30° is typical of geological materials in terrestrial conditions (Nedderman 2005). The duration for seismic shaking on the Moon was observed to be around 1 h. by the Apollo missions (Latham *et al.* 1970). In the absence of more precise constraints, we allow seismic effects to persist for this length of time in our simulations, which corresponds to $t \approx 2$ non-dimensional time units.

Once the landslide stops, grains are deposited on the body changing its overall shape. Subsequently, any new landslides mobilises a uniform regolith layer over this new shape. The body's rotational dynamics also incorporates its modified shape. We correspondingly update the Jacobian, curvatures and gravity for the body. All through, YORP torque continues to act. We take the YORP torque to be equal to that experienced by the asteroid Bennu were it is located in the main belt. To achieve this, the YORP torque was scaled by multiplying the torque experienced by Bennu (Hergenrother *et al.* 2019) by $(a_0/a)^2$, where $a_0 = 1.1$ AU is Bennu's original semi-major axis and $a = 2.3$ AU corresponds to that of an object located in the main belt (Bottke *et al.* 2015).

Before closing this section, we make the following observation. The YORP torque is very sensitive to variations in surface features (Statler 2009). Consequently, we should ideally account for spin evolution driven by YORP torque along with the modification of this torque due to reshaping, as done in the DE simulations of Cotto-Figueroa *et al.* (2015).

https://doi.org/10.1017/jfm.2026.11369 Published online by Cambridge University Press

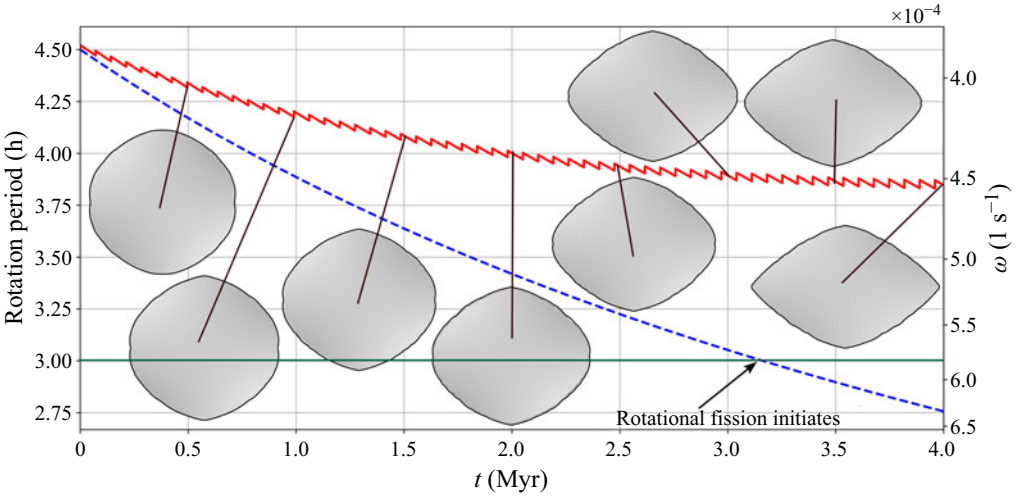


Figure 5. The evolution of the shape and rotation rate of an initially spherical rubble asteroid due to a constant YORP torque and impact-induced landslides over 4.0 Myr. The blue dashed curve tracks changes in the body's rotation rate when only the YORP torque is active.

Here, however, we focus on landslide-induced shape evolution and treat the YORP torque as constant. This is done to understand the importance of landslide-driven processes. Fully coupled models will be developed in the future.

4.2.2. *Results and discussion*

Figure 5 shows the evolution of the rotation rate and shape of an initially spherical asteroid over 4 Myr under the combined effects of a constant YORP torque and impact-induced global landsliding. Following the methodology described above, we estimate that the asteroid experiences 58 impacts large enough to initiate global landslides during this period. As noted earlier, these impacts are distributed uniformly over 4 Myr, and their occurrences are indicated by the spikes in the red curve in figure 5. The asteroid evolves into a top-shaped configuration, similar to the bodies shown in figure 1. Its shape is progressively modified by the deposition of multiple landslides, as illustrated schematically in figure 2(*b*).

The asteroid's rotation rate in figure 5 increases continuously under the YORP torque, while each landsliding event reduces this rate by redistributing regolith toward the equator, thereby increasing the body's moment of inertia. This feedback prevents the rotation rate from exceeding a critical limit. In contrast, the rotation rate under the action of the YORP torque alone – shown by the blue dashed curve in figure 5 – rises steadily. Along this curve the body's initial spherical shape is kept fixed. This continuous increase in the rotation rate will eventually lead to rotational fission, i.e. surface mass loss driven by centrifugal forces, when the rotation period drops below 3 h for our assumed density of 1250 kg/m^3 (Scheeres 2015). However, when landsliding effects are included, rotational fission is suppressed; indeed, the rotation period along the red curve in figure 5 remains above 3.75 h. This aspect is further probed in figure 7. We recall from (3.32*a*) that the basal pressure $p = \psi h$ must vanish for mass shedding. This is equivalent to the requirement (3.33) that $\psi < 0$. Figure 7 plots ψ at the equator at times when landsliding is absent, so that $\bar{\boldsymbol{u}} = \boldsymbol{0}$ in (3.32*b*). Under these conditions ψ functions as an effective gravity, comprising gravitational and centrifugal accelerations. We find that ψ at the equator

https://doi.org/10.1017/jfm.2026.11369 Published online by Cambridge University Press

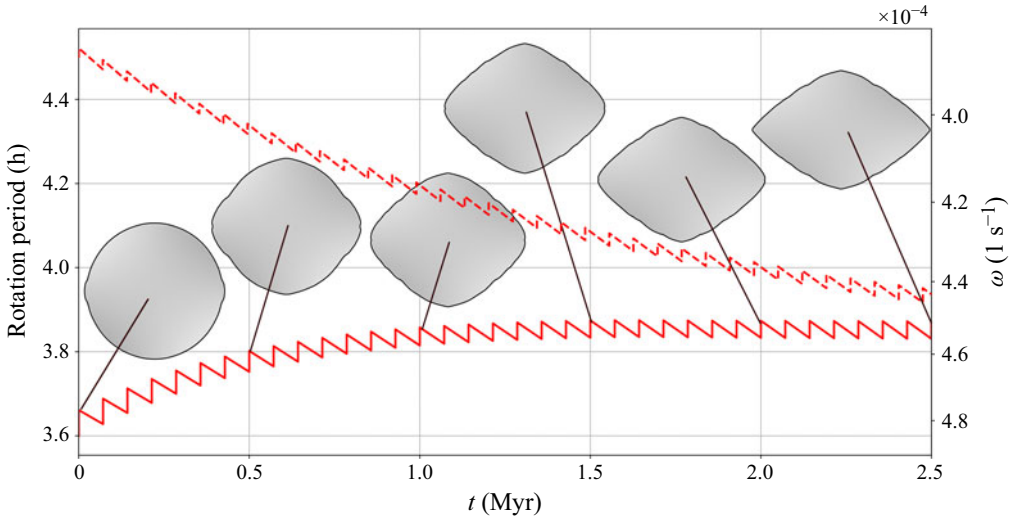


Figure 6. Same as figure 5 but the initial rotation period is decreased to 3.6 h. The dashed curve shows the spin evolution of figure 5.

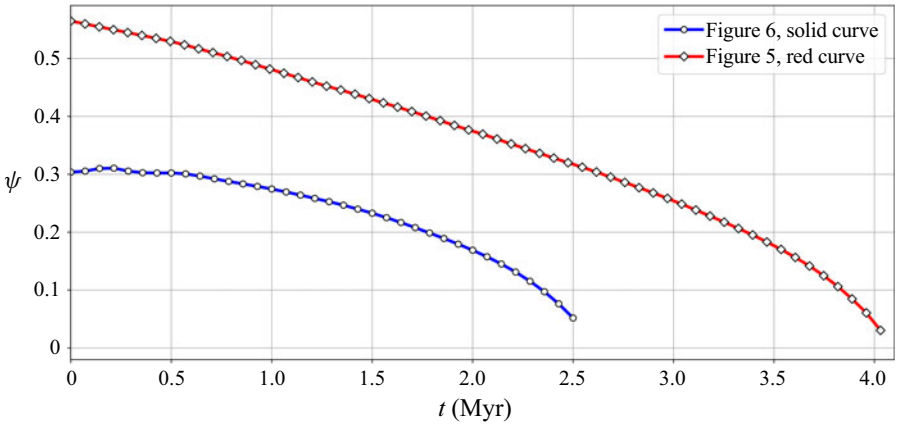


Figure 7. The change in ψ given by (3.32*b*) at the equator during the evolution of initially slow and fast rotating rubble asteroids reported in, respectively, figures 5 and 6.

remains positive during the body's evolution, confirming that mass shedding does not take place.

This result is significant, suggesting that rotational fission may be far less common – if it occurs at all – during the evolution of small rubble-pile bodies than is currently assumed. Finally, figure 5 shows that the asteroid's top-shaped form develops within a few Myr, which may account for the observed abundance of top-shaped asteroids in near-Earth orbits.

Figure 6 reproduces figure 5, except that the primordial body is initially rotating faster. For comparison, the rotation rate curve from the simulation in figure 5 is also included. We now find that the decrease in rotation rate caused by landsliding events dominates over the increase due to the YORP torque, resulting in a net lengthening of the rotation period. From figure 6, we infer that the shape changes induced by landslides – and hence their influence on the body's rotational dynamics – are more pronounced at higher rotation

https://doi.org/10.1017/jfm.2026.11369 Published online by Cambridge University Press

rates. Furthermore, figure 7 shows that, although the spin rate decreases in figure 6, ψ at the equator continues to decline. This behaviour is attributed to changes in the gravitational field resulting from the progressive elongation of the body's shape.

Comparing figures 5 and 6, we note that the final shapes are qualitatively similar. Moreover, the rotation rate curves in figure 6 appear to converge to nearly the same final value. We attribute this to the use of the same uniform distribution of impacts, so that landslides occur at identical times during the body's evolution. The outcome would differ if the impacts occurred randomly.

The evolution of ψ – the effective gravity – at the equator in figure 7 suggests that a continued increase in the angular velocity driven by the YORP effect and/or further bulging at the equator due to landsliding may eventually result in mass shedding from the equatorial region. Allowing for landsliding and the associated reshaping delays this mass shedding, which may be identified as 'rotational fission'. At the same time, we note that our model assumes that post-impact regolith mobilisation occurs uniformly over the surface. In reality, impacts are expected to preferentially mobilise larger volumes of regolith at higher elevations, which would act to suppress the equatorial bulge and, thereby, further delay the onset of mass shedding. We defer a quantitative investigation of this effect to future work.

Two technical points are worth noting. First, in the simulations of figures 5 and 6, the curvature ceases to remain small after a few Myr, violating the approximation in § 3.3 that curvatures are small. To address this, we employed the more accurate – and more complex – formulation given by (B6)–(B7), which retains all terms at $O(\varepsilon)$. Second, the simulations were terminated once the curvature near the equator became excessively large and mass shedding began.

We now connect our results with past work, focusing on studies that investigated surface mass motion. Harris *et al.* (2009) examined shape evolution driven by the movement of surface grains by considering the equilibrium of a single particle within the effective geopotential of a spinning body and its relocation once a local slope-stability criterion was violated. From this analysis, they derived axisymmetric equilibrium shapes that were successfully fitted to top-shaped asteroids. This work was extended by Scheeres (2015) to include spin changes due to the YORP torque and a more detailed treatment of post-failure regolith redistribution. It is interesting that some of the shapes observed during the evolution in figures 5 and 6 are similar to the ones reported in Scheeres (2015) figures 9, 10, and this lends support to both our approaches. Hirabayashi (2015), Hirabayashi *et al.* (2015) and Sánchez & Scheeres (2020) further developed this line of investigation to include cohesive grains, employing a combination of linear elasticity, and FE and DE simulations. An extension to irregular shapes was presented by Hirabayashi & Scheeres (2019). Collectively, these studies predicted the onset of failure due to increasing rotation rates from YORP torques and revealed the possibility of bulk failure preceding surface mobilisation when the interior is weak.

The above studies were essentially equilibrium analyses: they predicted the onset of failure, but did not follow the body's dynamical evolution after failure. Because of computational limitations, perhaps, they did not follow the long-term evolution of a rubble body's shape and spin state and, hence, could not comment on the time scales over which the body may achieve its final shape. They also focused on regolith flow triggered by centrifugal effects alone which, for a body with a strong interior, would mobilise only a small amount of surface material. In contrast, processes such as impact cratering may mobilise much larger volumes of regolith flows that, as shown here, will exert a significant influence on the body's rotational dynamics – to the extent that rotation rates may be suppressed at values well below those at which centrifugal effects can drive landslides.

https://doi.org/10.1017/jfm.2026.11369 Published online by Cambridge University Press

5. Conclusion

We have presented a framework for studying regolith motion on axisymmetric bodies that incorporates the effects of spin change, non-uniform gravity, varying topography and mass shedding. To achieve this, we extended depth-averaged flow models developed for terrestrial landslides. Our regolith flow model was coupled to the body's rotational dynamics while also tracking the changes in shape.

We applied this coupled framework to investigate regolith motion on axisymmetric shapes derived from real asteroids – Bennu, Ryugu and Itokawa. We also demonstrated our framework's ability to follow the shape and spin evolution of such bodies over long time scales relevant to planetary processes. The framework's strength lies in its capability to couple long-term dynamical evolution with numerous landsliding events, each resolved in detail. This would not be possible within current computational paradigms.

Initial investigations suggest two important findings. First, shape changes due to landsliding delay rotational fission, and sometimes even suppress it, challenging current understanding. Second, top-shaped bodies may form rapidly, over a few Myr, potentially explaining the observed overabundance of top-shaped NEAs. We are currently confirming these results through a statistically large set of simulations, in which key parameters, including the impact history of the body, will be systematically varied. It may even be possible to formulate scaling laws for the evolution time scale and the ratio of the maximum to minimum axes of the final shapes.

Several immediate extensions are apparent. First, DE simulations by Song *et al.* (2024) indicate that shed mass may re-impact the surface, whereas we currently assume that shed mass is lost to infinity. This likely overestimates mass loss and should be modelled more accurately. Next, relaxing the assumption of axisymmetry will allow us to address both small-scale, localised landslides triggered by impacts and bodies with more general shapes. We have also neglected the effect of cohesion. The DE simulations of Rognon *et al.* (2008) show that including cohesion effectively increases the friction coefficient μ, while also suppressing grain-shedding conditions (Sánchez & Scheeres 2020). Furthermore, in all our simulations, the initial landslide thickness was prescribed as spatially uniform. A more realistic estimate, linked to impact energy and its availability across the body, will be required to capture the variability of the thickness of the mobilised regolith.

Finally, we note the work of Deshpande *et al.* (2021), who showed that topography such as hillslopes may evolve via slow creeping motion even without external disturbances. However, their experiments were performed under terrestrial gravity, and this process is expected to be much slower and produce only limited displacement in a microgravity environment (Ballouz *et al.* 2019). Future work should compare the time scales of creeping motion with those of YORP-driven spin changes and the impact frequency, as well as its characteristic length scales with those of typical landslides.

Looking ahead, our framework may be readily adapted to analyse specific events. These include, for example, the effects of Earth's tidal forces on asteroid Apophis during its close encounter in 2029, or surface modifications on asteroid Didymos following the 2022 DART impact, which the Hera mission, launched in 2024, is set to investigate.

Acknowledgements. K.G. thanks financial support of the Prime Minister's Research Fellowship (PMRF) during his PhD. I.S. acknowledges MATRICS grant SERB/F/11747/2023-2024.

Declaration of interests. The authors report no conflicts of interest.

https://doi.org/10.1017/jfm.2026.11369 Published online by Cambridge University Press

Appendix A. Global angular momentum balance

Most quantities employed here have been defined in § 2 and figure 2. The angular momentum $\boldsymbol{H}_c$ of the central body about point P in figure 2 is given by

$$\boldsymbol{H}_c = \boldsymbol{R}_c \times M_c \boldsymbol{U}_c + \boldsymbol{I}_c \cdot \boldsymbol{\omega}, \tag{A1}$$

where $\boldsymbol{R}_c$ is the position vector of the centre of mass of the central body, $\boldsymbol{I}_c$ is the moment of inertia of the central body about C. Hence, the rate of change of the angular momentum $\boldsymbol{H}_c$ becomes

$$\frac{\mathrm{d}\boldsymbol{H}_c}{\mathrm{d}t} = \dot{M}_c \boldsymbol{R}_c \times \boldsymbol{U}_c + \boldsymbol{R}_c \times M_c \boldsymbol{A}_c + \boldsymbol{\omega} \times (\boldsymbol{I}_c \cdot \boldsymbol{\omega}) + \boldsymbol{I}_c \cdot \boldsymbol{\alpha} + \dot{\boldsymbol{I}}_c \cdot \boldsymbol{\omega}, \tag{A2}$$

where $\dot{(\,)}$ represents time differentiation in the body-fixed coordinate system. The angular momentum $\boldsymbol{H}_r$ of the regolith about P is given by

$$\boldsymbol{H}_r = \int \rho \boldsymbol{R} \times \boldsymbol{U} \mathrm{d}V, \tag{A3}$$

where $\boldsymbol{R} = \boldsymbol{R}_c + \boldsymbol{r}$ is the position vector of an infinitesimal regolith volume $\mathrm{d}V$ in $\mathcal{P}$ and $\boldsymbol{U}$ is the velocity of the regolith in the inertial frame that is given by $\boldsymbol{U} = \boldsymbol{U}_c + \boldsymbol{u} + \boldsymbol{\omega} \times \boldsymbol{r}$.

Employing (A3) we obtain

$$\frac{\mathrm{d}\boldsymbol{H}_r}{\mathrm{d}t} = \frac{\mathrm{d}}{\mathrm{d}t} \int \rho \boldsymbol{R} \times \boldsymbol{U} \mathrm{d}V = \frac{\mathrm{d}}{\mathrm{d}t} \left\{ \int \rho \boldsymbol{R}_c \times \boldsymbol{U} \mathrm{d}V + \int \rho \boldsymbol{r} \times (\boldsymbol{U}_c + \boldsymbol{u} + \boldsymbol{\omega} \times \boldsymbol{r}) \mathrm{d}V \right\}. \tag{A4}$$

Each term in the (A4) may be simplified as follows:

$$\frac{\mathrm{d}}{\mathrm{d}t} \int \rho \boldsymbol{R}_c \times \boldsymbol{U} \mathrm{d}V = \frac{\mathrm{d}}{\mathrm{d}t} (\boldsymbol{R}_c \times M_r \boldsymbol{U}_r) = \boldsymbol{U}_c \times M_r \boldsymbol{U}_r + \boldsymbol{R}_c \times \dot{M}_r \boldsymbol{U}_r + \boldsymbol{R}_c \times M_r \boldsymbol{A}_r, \tag{A5}$$

$$\frac{\mathrm{d}}{\mathrm{d}t} \int \rho \boldsymbol{r} \times \boldsymbol{U}_c \, \mathrm{d}V = \frac{\mathrm{d}}{\mathrm{d}t} \left\{ \int \rho (\boldsymbol{R} - \boldsymbol{R}_c) \times \boldsymbol{U}_c \, \mathrm{d}V \right\} = M_r \boldsymbol{U}_r \times \boldsymbol{U}_c + M_r \boldsymbol{r}_r \times \boldsymbol{A}_c + \dot{M}_r \boldsymbol{r}_r \times \boldsymbol{U}_c, \tag{A6}$$

$$\frac{\mathrm{d}}{\mathrm{d}t} \int \rho \boldsymbol{r} \times \boldsymbol{u} \mathrm{d}V = \frac{\mathrm{d}}{\mathrm{d}t} (\boldsymbol{h}_r) = \dot{\boldsymbol{h}}_r + \boldsymbol{\omega} \times \boldsymbol{h}_r \tag{A7}$$

and

$$\frac{\mathrm{d}}{\mathrm{d}t} \int \rho \boldsymbol{r} \times (\boldsymbol{\omega} \times \boldsymbol{r}) \mathrm{d}V = \frac{\mathrm{d}}{\mathrm{d}t} (\boldsymbol{I}_r \cdot \boldsymbol{\omega}) = \dot{\boldsymbol{I}}_r \cdot \boldsymbol{\omega} + \boldsymbol{I}_r \cdot \boldsymbol{\alpha} + \boldsymbol{\omega} \times (\boldsymbol{I}_r \cdot \boldsymbol{\omega}), \tag{A8}$$

where $\boldsymbol{r}_r$ is the position vector of the centre of mass of the regolith with respect to C,

$$\boldsymbol{I}_r = \int \rho \left(|\boldsymbol{r}|^2 \mathbf{1} - \boldsymbol{r} \otimes \boldsymbol{r} \right) \mathrm{d}V \tag{A9}$$

is the moment of inertia of the regolith about C and $\mathbf{1}$ is the identity tensor. Substituting (A1)–(A8) in the angular momentum balance (2.4) and employing (2.2), we obtain the final form of the global angular momentum balance

$$\boldsymbol{\omega} \times (\boldsymbol{I} \cdot \boldsymbol{\omega} + \boldsymbol{h}_r) + \boldsymbol{I} \cdot \boldsymbol{\alpha} + \dot{\boldsymbol{h}}_r + \dot{\boldsymbol{I}} \cdot \boldsymbol{\omega} + \boldsymbol{r}_r \times (M_r \boldsymbol{A}_c + \dot{M}_r \boldsymbol{U}_c) = \boldsymbol{T} - \boldsymbol{T}_s - \boldsymbol{R}_c \times (\boldsymbol{F} - \boldsymbol{F}_s), \tag{A10}$$

where $\boldsymbol{h}_r$ is the angular momentum of the flowing regolith about C in $\mathcal{E}_0$ and $\boldsymbol{I}$ is the moment of inertia about C of the system comprising the central body and the flowing regolith. If we take the location and velocity of the inertial frame to coincide with that of

https://doi.org/10.1017/jfm.2026.11369 Published online by Cambridge University Press

the body-fixed coordinate system, then $\boldsymbol{R}_c = \boldsymbol{U}_c = 0$ and $M_r \boldsymbol{r}_r = M\boldsymbol{R}_O$, where M and $\boldsymbol{R}_O$ are, respectively, the total system mass and the location of its centre of mass with respect to C. These simplifications reduce the angular momentum balance (A10) to (2.4).

Appendix B. Axisymmetric equations including $O(\varepsilon)$ terms

For completeness, we provide here depth-averaged equations for regolith flow that include the constitutive law (3.30), the effect of curvature variations and where we do not make the traditional approximation, i.e. we retain the contributions from Coriolis forces in their entirety. The depth-averaged axisymmetric equations then become

$$
\begin{gathered}
J^s \frac{\partial h}{\partial t} + \frac{\partial}{\partial \theta}\left(\overline{\mathcal{R}_\phi u_\theta} h\right) = 0 \\
\frac{\partial}{\partial t}\left(\overline{J^2 \kappa_\phi u_\theta} h\right) + \frac{\partial}{\partial \theta}\left(\overline{J A_{\theta\theta}} h\right) - \overline{\frac{\partial}{\partial \theta}\left(J\kappa_\phi\right)\frac{A_{\theta\theta}}{\kappa_\phi}} h - \overline{J^2 \kappa_\phi \kappa_{\phi g} A_{\phi\phi}} h = -\mu (J^b)^2 \kappa_\phi^b \hat{u}_\theta^b \sigma_{nn}^b + \overline{J^2 \kappa_\phi f_\theta} h \\
\text{and} \quad \frac{\partial}{\partial t}\left(\overline{J \mathcal{R}_\phi u_\phi} h\right) + \frac{\partial}{\partial \theta}\left(\overline{\mathcal{R}_\phi^2 A_{\theta\phi}} h\right) = -\mu (J^b)^2 \kappa_\phi^b \hat{u}_\phi^b \sigma_{nn}^b + \overline{J \mathcal{R}_\phi f_\phi} h. \qquad \text{(B1)}
\end{gathered}
$$

The depth-averaged quantities depend on the velocity profile. For our case, we assume the velocity profile to be nearly constant in the normal direction i.e. $u_i = \bar{u}_i + O(\varepsilon)$. Because the Jacobian and the curvatures also vary as $J = J^b + O(\varepsilon)$ and $\kappa_i = \kappa_i^b + O(\varepsilon)$, we may write all depth-averaged terms as $\overline{AB} = \overline{A}\,\overline{B} + O(\varepsilon^2)$. Employing these depth-averaged quantities (B1) become

$$
\begin{gathered}
\frac{\partial}{\partial t}\left(\overline{J} h\right) + \frac{\partial}{\partial \theta}\left(\overline{\mathcal{R}}_\phi \bar{u}_\theta h\right) = 0, \\
\frac{\partial}{\partial t}\left(\overline{J^2 \kappa}_\phi \bar{u}_\theta h\right) + \frac{\partial}{\partial \theta}\left(\overline{J}\,\overline{A}_{\theta\theta} h\right) = -\mu (J^b)^2 \kappa_\phi^b \hat{u}_\theta^b \sigma_{nn}^b + \overline{\frac{\partial}{\partial \theta}\left(J\kappa_\phi\right)} \overline{\mathcal{R}}_\phi \overline{A}_{\theta\theta} h + \overline{J}^2 \overline{\kappa}_\phi \left(\overline{\kappa}_{\phi g} \overline{A}_{\phi\phi} + \overline{f}_\theta\right) h \\
\text{and} \quad \frac{\partial}{\partial t}\left(\overline{J}\,\overline{\mathcal{R}}_\phi \bar{u}_\phi h\right) + \frac{\partial}{\partial \theta}\left(\overline{\mathcal{R}}_\phi^2 \overline{A}_{\theta\phi} h\right) = -\mu J^b \mathcal{R}_\phi^b \hat{u}_\phi^b \sigma_{nn}^b + \overline{J}\,\overline{\mathcal{R}}_\phi \overline{f}_\phi h. \qquad \text{(B2)}
\end{gathered}
$$

Decomposing the stress field as $\sigma_{ij} = -p\delta_{ij} + \tilde{\sigma}_{ij}$, we may write

$$
p = \tilde{\sigma}_{nn} + \psi(h - n) + O(\varepsilon). \qquad \text{(B3)}
$$

Because the deviatoric stress tensor is traceless, we may substitute $\tilde{\sigma}_{nn} = -(\tilde{\sigma}_{\theta\theta} + \tilde{\sigma}_{\phi\phi})$. Now expanding each term in (B2)

$$
\begin{aligned}
&\overline{J} = J^b\left[1 + \varepsilon\left(\kappa_\theta^b + \kappa_{\phi n}^b\right)\frac{h}{2}\right] + O(\varepsilon^2), && \overline{\mathcal{R}}_\phi = \mathcal{R}_\phi^b\left(1 + \varepsilon \kappa_{\phi n}^b \frac{h}{2}\right) + O(\varepsilon^2) \\
&\overline{\kappa}_{\phi g} = \kappa_{\phi g}^b\left(1 - \varepsilon \kappa_{\phi n}^b \frac{h}{2}\right) + O(\varepsilon^2), && \overline{\kappa}_{\phi n} = \kappa_{\phi n}^b\left(1 - \varepsilon \kappa_{\phi n}^b \frac{h}{2}\right) + O(\varepsilon^2) \\
&\overline{A}_{\theta\theta} = \bar{u}_\theta^2 + \varepsilon\left(\frac{\psi h}{2} - 2\overline{\tilde{\sigma}}_{\theta\theta} - \overline{\tilde{\sigma}}_{\phi\phi}\right), && \overline{A}_{\phi\phi} = \bar{u}_\phi^2 + \varepsilon\left(\frac{\psi h}{2} - 2\overline{\tilde{\sigma}}_{\phi\phi} - \overline{\tilde{\sigma}}_{\theta\theta}\right), \\
&\overline{A}_{\theta\phi} = \bar{u}_\theta \bar{u}_\phi + \varepsilon \overline{\sigma}_{\theta\phi}, && \overline{\frac{\partial}{\partial \theta}\left(J\kappa_\phi\right)} = \frac{\partial}{\partial \theta}\left(J^b \kappa_\phi^b\right) + \varepsilon \frac{\partial}{\partial \theta}\left(J^b \kappa_\phi^b \kappa_\theta^b\right)\frac{h}{2}, \\
&\overline{f}_\theta = \overline{b}_\theta + \overline{\mathcal{R}}_\phi \overline{\kappa}_{\phi g}\left(\overline{\mathcal{R}}_\phi \omega^2 + 2\omega \bar{u}_\phi\right), && \overline{f}_\phi = -\overline{\mathcal{R}}_\phi\left(2\omega(\varepsilon \overline{\kappa}_{\phi n} \bar{u}_n + \overline{\kappa}_{\phi g} \bar{u}_\theta) + \alpha\right),
\end{aligned}
$$

https://doi.org/10.1017/jfm.2026.11369 Published online by Cambridge University Press

$$\overline{b}_\theta = b^b_\theta + \frac{\varepsilon}{\overline{J}\,\overline{\kappa}_\phi}\frac{\partial b^b_n}{\partial\theta}\frac{h}{2} + O(\varepsilon^2), \qquad \overline{u}_n = -\frac{h}{2\overline{J}}\frac{\partial}{\partial\theta}\left(\overline{\mathcal{R}}_\phi\overline{u}_\theta\right) + O(\varepsilon),$$

$$\overline{\tilde{\sigma}}_{\theta\theta} = \frac{\nu}{b}h^{1/2}\frac{\mathcal{R}^b_\phi}{J^b}\frac{\partial\overline{u}_\theta}{\partial\theta} + O(\varepsilon), \qquad \overline{\tilde{\sigma}}_{\phi\phi} = \frac{\nu}{b}h^{1/2}\kappa^b_{\phi g}\overline{u}_\theta + O(\varepsilon)$$

$$\text{and}\quad \overline{\tilde{\sigma}}_{\theta\phi} = \frac{\nu}{b}h^{1/2}\frac{\left(\mathcal{R}^b_\phi\right)^2}{2J^b}\frac{\partial}{\partial\theta}\left(\frac{\overline{u}_\phi}{\mathcal{R}^b_\phi}\right) + O(\varepsilon). \tag{B4}$$

By substituting the above relations into (B2), we obtain the depth-averaged equations that incorporate all contributions up to $O(\varepsilon)$. The resulting system, which includes the $O(\varepsilon)$ corrections from curvature, gravity and Coriolis effects, is

$$\frac{\partial}{\partial t}\left(\overline{J}h\right) + \frac{\partial}{\partial\theta}\left(\overline{\mathcal{R}}_\phi\bar{u}_\theta h\right) = 0, \tag{B5}$$

$$\frac{\partial}{\partial t}\left(\overline{J}^2\overline{\kappa}_\phi\bar{u}_\theta h\right) + \frac{\partial}{\partial\theta}\left(\overline{J}\left(\overline{u}^2_\theta + \varepsilon\psi\frac{h}{2}\right)h\right) = \overline{J}^2\overline{\kappa}_\phi h\left[\overline{\kappa}_{\phi g}\overline{U}^2_\phi + b^b_\theta + \frac{\varepsilon}{\overline{J}\,\overline{\kappa}_\phi}\frac{\partial b^b_n}{\partial\theta}\frac{h}{2}\right]\ldots$$
$$\ldots - (J^b)^2\mu\kappa^b_\phi\hat{u}^b_\theta\psi h + \left[\frac{\partial}{\partial\theta}\left(J^b\kappa^b_\phi\right) + \varepsilon\frac{\partial}{\partial\theta}\left(J^b\kappa^b_\phi\kappa^b_\theta\right)\frac{h}{2}\right]\overline{\mathcal{R}}_\phi\overline{u}^2_\theta h + \frac{\varepsilon}{2}\frac{\partial J^b}{\partial\theta}\psi h^2 \tag{B6}$$

$$\text{and}\quad \frac{\partial}{\partial t}\left(\overline{J}\,\overline{\mathcal{R}}_\phi\overline{U}_\phi h\right) + \frac{\partial}{\partial\theta}\left(\overline{\mathcal{R}}^2_\phi\overline{U}_\phi\overline{u}_\theta h\right) = -\mu J^b\mathcal{R}^b_\phi\hat{u}^b_\phi\psi h. \tag{B7}$$

The above set of equations was used to generate figures 5 and 6.

Appendix C. Energy balance

The linear momentum balance (3.35) and (3.36) is in the conservative form that expresses the rate of change of conserved quantities, respectively, linear momentum in the $\theta-$direction and angular momentum about the symmetry axis. Employing the continuity (3.34) we may write (3.35) and (3.36) in terms of primitive variables $\bar{u}_\theta$ and $\bar{U}_\phi$ as

$$\frac{\partial\bar{u}_\theta}{\partial t} + \frac{\mathcal{R}_\phi\bar{u}_\theta}{J}\frac{\partial\bar{u}_\theta}{\partial\theta} + \frac{\varepsilon\mathcal{R}_\phi}{2Jh}\frac{\partial}{\partial\theta}\left(\psi h^2\right) = -\mu\psi\hat{\bar{u}}_\theta + b^0_\theta + \kappa_{\phi g}\bar{U}^2_\phi, \tag{C1}$$

$$\text{and}\qquad \frac{\partial\bar{U}_\phi}{\partial t} + \frac{\mathcal{R}_\phi\bar{u}_\theta}{J}\frac{\partial\bar{U}_\phi}{\partial\theta} = -\kappa_{\phi g}\bar{u}_\theta\bar{U}_\phi - \mu\psi\hat{\bar{u}}_\phi. \tag{C2}$$

Multiplying (C1) and (C2) by, respectively, $\bar{u}_\theta$ and $\bar{U}_\phi$, and adding, we find

$$\frac{\partial}{\partial t}\left(\frac{|\bar{U}|^2}{2}\right) + \frac{\mathcal{R}_\phi\bar{u}_\theta}{J}\frac{\partial}{\partial\theta}\left(\frac{|\bar{U}|^2}{2}\right) + \frac{\varepsilon\mathcal{R}_\phi\bar{u}_\theta}{2Jh}\frac{\partial}{\partial\theta}\left(\psi h^2\right) = -\mu\psi\left(|\bar{u}|^2 + \mathcal{R}_\phi\omega\hat{\bar{u}}_\phi\right) + b^0_\theta\bar{u}_\theta, \tag{C3}$$

where $|\bar{U}|^2 = \sqrt{\bar{U}^2_\theta + \bar{U}^2_\phi}$, $|\bar{u}|^2 = \sqrt{\bar{u}^2_\theta + \bar{u}^2_\phi}$ and we have noted that $\bar{u}_\theta = \bar{U}_\theta$. The tangential gravitational body force b^0_θ may be obtained from the gravitational potential at the surface $V(\theta)$

$$b^0_\theta = -\boldsymbol{\nabla}V(\theta)\cdot\hat{\boldsymbol{g}}_2 = -\frac{\mathcal{R}_\phi}{J}\frac{\partial V(\theta)}{\partial\theta}. \tag{C4}$$

https://doi.org/10.1017/jfm.2026.11369 Published online by Cambridge University Press

Combining (3.34) and (C3) after multiplying them by, respectively, $(|\bar{U}|^2 + V(\theta) - \varepsilon b_n^0 h)$ and Jh, we arrive at the energy equation

$$\frac{\partial}{\partial t}(JEh) + \frac{\partial}{\partial \theta}\left\{\left(E - \frac{\varepsilon}{2} b_n^0 h\right)\mathcal{R}_\phi \bar{u}_\theta h\right\} = -\mu J \psi h\left(|\bar{u}| + \mathcal{R}_\phi \omega \hat{\bar{u}}_\phi\right) - \varepsilon \mathcal{R}_\phi \bar{u}_\theta \left\{h \frac{\partial}{\partial \theta}\left(b_n^0 h\right) + \frac{\partial}{\partial \theta}\left(\frac{\psi h^2}{2}\right)\right\}, \quad \text{(C5)}$$

where

$$E = \frac{|\bar{U}|^2}{2} + V(\theta) - \varepsilon b_n^0 \frac{h}{2} \quad \text{(C6)}$$

is the energy density. The above balance shows that the total energy of the flowing regolith is changed by basal friction and an extra $O(\varepsilon)$ source term that is present because we have neglected $O(\varepsilon)$ contributions to the curvature while depth averaging; see § 3.3. Indeed, following the steps above, we may obtain the energy balance for the system of (B5)–(B7), which includes $\mathcal{O}(\varepsilon)$ terms, as

$$\frac{\partial}{\partial t}\left\{\bar{J} E h\right\} + \frac{\partial}{\partial \theta}\left\{\left(E + \varepsilon \psi \frac{h}{2}\right)\bar{\mathcal{R}}_\phi \bar{u}_\theta h\right\} = -\mu \bar{J} \psi h\left(|\bar{u}| + \bar{\mathcal{R}}_\phi \omega \hat{\bar{u}}_\phi\right). \quad \text{(C7)}$$

Appendix D. Code validation

We performed the following to validate our governing equations and numerical scheme.

(i) Reduction to standard shallow water flow on sphere. By substituting

$$\mathcal{R}_\theta = R_0, \quad \mathcal{R}_\phi = R_0 \sin\theta, \quad \kappa_{\phi g} = \frac{1}{R_0 \tan\theta} \quad \text{and} \quad \kappa_{\phi n} = \frac{1}{R} \quad \text{(D1)}$$

in the frictionless form of the (3.34)–(3.36), assuming hydrostatic pressure and spherical geopotentials, we recover the axisymmetric version of the hydrostatic primitive equations. These are employed to simulate atmospheric flows on aspherical Earth (Williamson & Browning 1973; White *et al.* 2005).

(ii) Conservation of geopotential profile. If the initial height profile of frictionless regolith coincides with a geopotential surface, the material should remain stationary. To test this, we adopted a spherical central body with the parameters listed in table 1 and imposed a rotation period of 10 h. The initial regolith surface was then prescribed to lie on the geopotential surface of the sphere defined by

$$-\frac{GM}{r} - \frac{1}{2}\omega^2 r^2 \sin^2\theta = C_1, \quad \text{(D2)}$$

where M is the mass of the central body, r is the radial distance to the geopotential surface and C_1 is chosen so that the regolith volume matches the volume enclosed between the sphere and the geopotential surface. In regions where the computed r falls below the sphere's radius R, we set $r = R$ to avoid negative regolith thickness. This profile was then placed on the rotating sphere and evolved for a non-dimensional time of $t = 50$. The resulting surface, shown in figure 8(*a*) by dashed blue curve, indicates that the initial regolith configuration remains unchanged throughout the simulation.

(iii) Flow of uniform frictionless regolith layer. The final deposit shape is expected to approximate a geopotential surface for nearly frictionless grains. To examine this, we evolved a uniform layer of nearly frictionless regolith modelled using a very small

https://doi.org/10.1017/jfm.2026.11369 Published online by Cambridge University Press

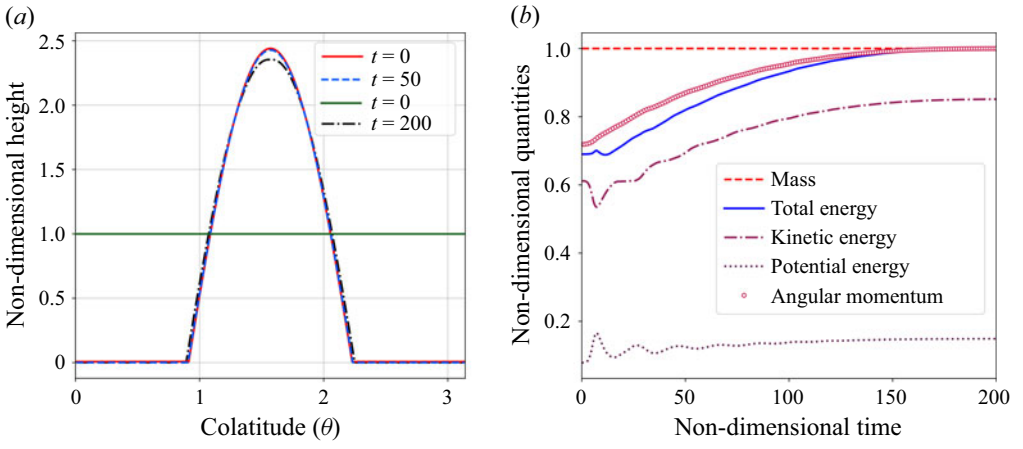


Figure 8. (*a*) The final regolith profiles for two different initial profiles, *viz.* a geopotential surface (red) and a uniform-height layer (green). The corresponding final profiles are shown by, respectively, blue and black dashed curves. The geopotential surface corresponds to a spherical asteroid with parameters in table 1 and a rotation period of 10 hours, and the regolith had a friction angle of $\zeta = 0°$. The uniform regolith layer had a small friction angle of $\zeta = 0.1°$. (*b*) Time evolution of various quantities in the simulation corresponding to the regolith flow beginning with a uniform initial height in (*a*).

friction angle $\zeta = 0.1°$, with the initial condition (4.1) on the rotating spherical body described in the previous item. Figure 8(*a*) compares the resulting final profile (dot-dashed black curve) at $t = 200$ with a geopotential surface of equal volume, revealing a close agreement. The slight discrepancies arise from the small, but finite friction angle, and from numerical diffusion, which diminishes the peak height when the simulation is run for an extended duration.

(iv) Mass conservation. Mass should be conserved throughout the simulation, unless mass is lost due to shedding. As shown in figures 8(*b*) and 9, the mass of the regolith is consistently conserved.

(v) Angular momentum conservation. The angular momentum of the regolith is conserved when friction is absent, as may be seen from (B7). However, when friction is present, the basal friction drives an azimuthal flow, which modifies the angular momentum of the regolith. In this scenario, only the total angular momentum of the system consisting of the flowing regolith and the central body would be conserved. The latter aspect is displayed in figure 8(*b*). Indeed, the angular momentum of the regolith is found to increase. On the other hand, the angular momentum for frictionless grains in figure 9 remains constant.

(vi) Total energy conservation in the inertial frame. The total energy of the regolith in the inertial frame should be non-increasing when friction is absent, which is demonstrated in figure 9. Energy may decrease due to numerical viscosity, especially when high gradients – shocks – form. These shocks are also displayed in the inset of figure 9, corresponding to the sudden decrease in the total energy. Once the shocks have subsided the total energy remains nearly constant as the effects of numerical viscosity become small, although we continue to observe exchange of energies between potential and kinetic terms in (C7). In contrast, in figure 8(*b*), as expected from (C7), the total energy increases because of the presence of the small basal frictional term.

https://doi.org/10.1017/jfm.2026.11369 Published online by Cambridge University Press

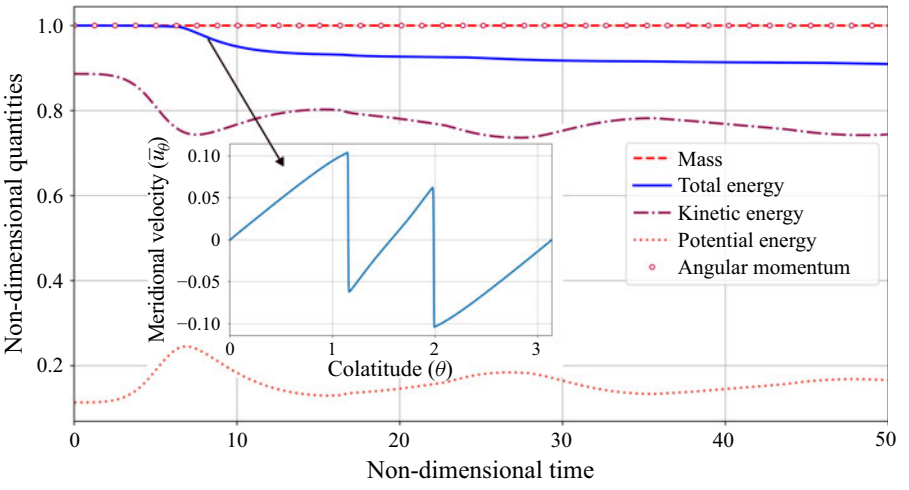


Figure 9. Same as figure 8(*b*), but for zero friction angle $\zeta = 0°$. The inset in the figure shows shocks in the meridional velocity that lead to energy dissipation.

References

Baker, J.L., Barker, T. & Gray, J.M.N.T. 2016 A two-dimensional depth-averaged-rheology for dense granular avalanches. *J. Fluid Mech.* **787**, 367–395.

Ballouz, R.-L., Baresi, N., Crites, S.T., Kawakatsu, Y. & Fujimoto, M. 2019 Surface refreshing of Martian moon phobos by orbital eccentricity-driven grain motion. *Nat. Geosci.* **12** (4), 229–234.

Banik, D., Gaurav, K. & Sharma, I. 2022 Regolith flow on top-shaped asteroids. *Proc. R. Soc. Lond. A.* **478** (2262), 20210972.

Barnouin, O.S.The OSIRIS-REx Team 2019 Shape of (101955) Bennu indicative of a rubble pile with internal stiffness. *Nat. Geosci.* **12** (4), 247–252.

Bottke, W.F., Vokrouhlickỳ, D., Walsh, K.J., Delbo, M., Michel, P., Lauretta, D.S., Campins, H., Connolly, H.C.Jr Scheeres, D.J. & Chelsey, S.R. 2015 In search of the source of asteroid (101955) bennu: applications of the stochastic YORP model. *Icarus* **247**, 191–217.

Bouchut, F. & Westdickenberg, M. 2004 Gravity driven shallow water models for arbitrary topography. *Commun. Math. Sci* **2** (3), 359–389.

Brack, D.N. & McMahon, J.W. 2019 Modeling the coupled dynamics of an asteroid with surface boulder motion. *Icarus* **333**, 96–112.

Breiter, S., Rożek, A. & Vokrouhlickỳ, D. 2012 Stress field and spin axis relaxation for inelastic triaxial ellipsoids. *Mon. Not. R. Astron. Soc.* **427** (1), 755–769.

Burns, J.A., Safronov, V.S. & Gold, T. 1973 Asteroid nutation angles. *Mon. Not. R. Astron. Soc.* **165** (4), 403–411.

Cheng, B., Yu, Y., Asphaug, E., Michel, P., Richardson, D.C., Hirabayashi, M., Yoshikawa, M. & Baoyin, H. 2021 Reconstructing the formation history of top-shaped asteroids from the surface boulder distribution. *Nat. Astron.* **5** (2), 134–138.

Cotto-Figueroa, D., Statler, T.S., Richardson, D.C. & Tanga, P. 2015 Coupled spin and shape evolution of small rubble-pile asteroids: self-limitation of the YORP effect. *Astrophys. J.* **803** (1), 25.

Deshpande, N.S., Furbish, D.J., Arratia, P.E. & Jerolmack, D.J. 2021 The perpetual fragility of creeping hillslopes. *Nat. Commun.* **12** (1), 3909.

Eckart, C. 1960 *Hydrodynamics of Oceans and Atmospheres*. Pergamon.

Gaurav, K., Banik, D., Sharma, I. & Dutt, P. 2021 Granular flow on a rotating and gravitating elliptical body. *J. Fluid Mech.* **916**, A40.

Gerkema, T., Zimmerman, J.T.F., Maas, L.R.M. & Van Haren, H. 2008 Geophysical and astrophysical fluid dynamics beyond the traditional approximation. *Rev. Geophys.* **46** (2).

Ghosh, S., Sharma, I. & Dhingra, D. 2024 Segregation on small rubble bodies due to impact-induced seismic shaking. *Proc. R. Soc. Lond. A.* **480** (2292), 20230715.

Gray, J.M.N.T. & Edwards, A.N. 2014 A depth-averaged-rheology for shallow granular free-surface flows. *J. Fluid Mech.* **755**, 503–534.

https://doi.org/10.1017/jfm.2026.11369 Published online by Cambridge University Press

GRAY, J.M.N.T., WIELAND, M. & HUTTER, K. 1999 Gravity-driven free surface flow of granular avalanches over complex basal topography. *Proc. R. Soc. Lond. A.* **455**(1985), 1841–1874.
HARRIS, A.W., FAHNESTOCK, E.G. & PRAVEC, P. 2009 On the shapes and spins of 'rubble pile' asteroids. *Icarus* **199** (2), 310–318.
HERGENROTHER, C.W., MALESZEWSKI, C.K., NOLAN, M.C., LI, J-Y., DROUET D'AUBIGNY, C.Y., HOWELL, E.S., KARETA, T.R., IZAWA, M.R.M. & BARUCCI, M.A. 2019 The operational environment and rotational acceleration of asteroid (101955) Bennu from OSIRIS-REx observations. *Nat. Commun.* **10** (1), 1291.
HESTROFFER, D., *et al.* 2019 Small solar system bodies as granular media. *Astron. Astrophys. Rev.* **27**, 1–64.
HIRABAYASHI, M. 2015 Failure modes and conditions of a cohesive, spherical body due to YORP spin-up. *Mon. Not. R. Astron. Soc.* **454** (2), 2249–2257.
HIRABAYASHI, M., SÁNCHEZ, D.P. & SCHEERES, D.J. 2015 Internal structure of asteroids having surface shedding due to rotational instability. *Astrophys. J.* **808** (1), 63.
HIRABAYASHI, M. & SCHEERES, D.J. 2019 Rotationally induced failure of irregularly shaped asteroids. *Icarus* **317**, 354–364.
HOLSAPPLE, K.A. 2022 Main belt asteroid collision histories: cratering, ejecta, erosion, catastrophic dispersions, spins, binaries, tops, and wobblers. *Planet. Space Sci.* **219**, 105529.
HUANG, C., YU, Y., CHENG, B. & WANG, Q. 2022 Long-term trends of regolith movement on the surface of small bodies. *Nonlinear Dyn.* **110** (3), 2283–2296.
HURÉ, J.-M. 2012 A key-formula to compute the gravitational potential of inhomogeneous discs in cylindrical coordinates. *Celest. Mech. Dyn. Astron.* **114** (4), 365–385.
JAWIN, E.R., WALSH, K.J., BARNOUIN, O.S., MCCOY, T.J., BALLOUZ, R-L., DELLAGIUSTINA, D.N., CONNOLLY, JR, BEDDINGFIELD, C. & NOLAN, M.C. 2020 Global patterns of recent mass movement on asteroid (101955) Bennu. *J. Geophys. Res. Planets* **125** (9), e2020JE006475.
JIANG, Y., ZHANG, Y. & BAOYIN, H. 2016 Surface motion relative to the irregular celestial bodies. *Planet. Space Sci.* **127**, 33–43.
KURGANOV, A. & TADMOR, E. 2000 New high-resolution central schemes for nonlinear conservation laws and convection–diffusion equations. *J. Comput. Phys.* **160** (1), 241–282.
LATHAM, G.V., EWING, M., PRESS, F., SUTTON, G., DORMAN, J., NAKAMURA, Y., TOKSÖZ, N., WIGGINS, R., DERR, J. & DUENNEBIER, F. 1970 Passive seismic experiment. *Science* **167** (3918), 455–457.
LUCA, I., TAI, Y.-C. & KUO, C.-Y. 2016 *Shallow Geophysical Mass Flows Down Arbitrary Topography*. Springer Cham.
MELOSH, H.J. 1986 The physics of very large landslides. *Acta Mechanica* **64** (1), 89–99.
MIYAMOTO, H., YANO, H., SCHEERES, D.J., ABE, S., BARNOUIN-JHA, O., CHENG, A.F., DEMURA, H., GASKELL, R.W., HIRATA, N. & ISHIGURO, M. 2007 Regolith migration and sorting on asteroid itokawa. *Science* **316** (5827), 1011–1014.
NEDDERMAN, R.M. 2005 *Statics and Kinematics of Granular Materials*. Cambridge University Press.
PUDASAINI, S.P. & HUTTER, K. 2007 *Avalanche Dynamics*. Springer Science & Business Media.
QUILLEN, A.C., ZHAO, Y., CHEN, Y., SANCHEZ, P., NELSON, R.C. & SCHWARTZ, S.R. 2019 Impact excitation of a seismic pulse and vibrational normal modes on asteroid Bennu and associated slumping of regolith. *Icarus* **319**, 312–333.
RICHARDSON, J.E., MELOSH, H.J., GREENBERG, R.J. & O'BRIEN, D.P. 2005 The global effects of impact-induced seismic activity on fractured asteroid surface morphology. *Icarus* **179** (2), 325–349.
ROCHA, F.M., JOHNSON, C.G. & GRAY, J.M.N.T. 2019 Self-channelisation and levee formation in monodisperse granular flows. *J. Fluid Mech.* **876**, 591–641.
ROGNON, P.G., ROUX, J., NAAIM, M. & CHEVOIR, F. 2008 Dense flows of cohesive granular materials. *J. Fluid Mech.* **596**, 21–47.
SÁNCHEZ, D.P. & SCHEERES, D.J. 2012 DEM simulation of rotation-induced reshaping and disruption of rubble-pile asteroids. *Icarus* **218** (2), 876–894.
SÁNCHEZ, P. & SCHEERES, D.J. 2020 Cohesive regolith on fast rotating asteroids. *Icarus* **338**, 113443.
SAVAGE, S.B. & HUTTER, K. 1989 The motion of a finite mass of granular material down a rough incline. *J. Fluid Mech.* **199**, 177–215.
SCHEERES, D.J. 2015 Landslides and mass shedding on spinning spheroidal asteroids. *Icarus* **247**, 1–17.
SHARMA, I. 2017 *Shapes and Dynamics of Granular Minor Planets*. Springer.
SHARMA, I., BURNS, J.A. & HUI, C.-Y. 2005 Nutational damping times in solids of revolution. *Mon. Not. R. Astron. Soc.* **359** (1), 79–92.
SONG, Z., YU, Y., SOLDINI, S., CHENG, B. & MICHEL, P. 2024 An integrated DEM code for tracing the entire regolith mass movement on asteroids. *Mon. Not. R. Astron. Soc.* **532** (2), 1307–1329.

https://doi.org/10.1017/jfm.2026.11369 Published online by Cambridge University Press

STATLER, T.S. 2009 Extreme sensitivity of the YORP effect to small-scale topography. *Icarus* **202** (2), 502–513.

SUGITA, S., HONDA, R., MOROTA, T., KAMEDA, S., SAWADA, H., TATSUMI, E., YAMADA, M., HONDA, C., YOKOTA, Y. & KOUYAMA, T. 2019 The geomorphology, color, and thermal properties of ryugu: implications for parent-body processes. *Science* **364** (6437), eaaw0422.

SUGIURA, K., KOBAYASHI, H., WATANABE, S., GENDA, H., HYODO, R. & INUTSUKA, S. 2021 SPH simulations for shape deformation of rubble-pile asteroids through spinup: the challenge for making top-shaped asteroids Ryugu and Bennu. *Icarus* **365**, 114505.

TANG, Y., LAURETTA, D.S., BALLOUZ, R.-L., DELLAGIUSTINA, D.N., BENNETT, C.A., WALSH, K.J. & GOLISH, D.R. 2023 Simulating impact-induced shaking as a triggering mechanism for mass movements on Bennu. *Icarus* **395**, 115463.

TARDIVEL, S., SÁNCHEZ, P. & SCHEERES, D.J. 2018 Equatorial cavities on asteroids, an evidence of fission events. *Icarus* **304**, 192–208.

VOKROUHLICKÝ, D., BOTTKE, W.F., CHESLEY, S.R., SCHEERES, D.J. & STATLER, T.S. 2015 *The Yarkovsky and YORP Effects*, pp. 509–532. University of Arizona Press.

VOKROUHLICKỲ, D., MILANI, A. & CHESLEY, S.R. 2000 Yarkovsky effect on small near-earth asteroids: mathematical formulation and examples. *Icarus* **148** (1), 118–138.

WALSH, K.J. 2018 Rubble pile asteroids. *Annu. Rev. Astron. Astrophys.* **56** (1), 593–624.

WALSH, K.J., RICHARDSON, D.C. & MICHEL, P. 2008 Rotational breakup as the origin of small binary asteroids. *Nature* **454** (7201), 188–191.

WATANABE, S.The OSIRIS-REx Team 2019 Hayabusa2 arrives at the carbonaceous asteroid 162173 Ryugu – a spinning top–shaped rubble pile. *Science* **364** (6437), 268–272.

WHITE, A.A., HOSKINS, B.J., ROULSTONE, I. & STANIFORTH, A. 2005 Consistent approximate models of the global atmosphere: shallow, deep, hydrostatic, quasi-hydrostatic and non-hydrostatic. *Q. J. R. Meteorol. Soc.* **131** (609), 2081–2107.

WILLIAMSON, D.L. & BROWNING, G.L. 1973 Comparison of grids and difference approximations for numerical weather prediction over a sphere. *J. App. Meteorol.* **1962**, 264–274.

ZHANG, Y., ZENG, X., CIRCI, C. & VULPETTI, G. 2019 The motion of surface particles for the asteroid 101955 Bennu. *Acta Astronaut.* **163**, 3–10.

https://doi.org/10.1017/jfm.2026.11369 Published online by Cambridge University Press